

Bridging the gap between airborne and spaceborne imaging spectroscopy for mountain glacier surface property retrievals



Christopher P. Donahue ^{a,b,*}, Brian Menounos ^{a,b,*}, Nick Viner ^b, S. McKenzie Skiles ^c, Steven Beffort ^b, Taylor Denoudin ^b, Santiago Gonzalez Arriola ^b, Robert White ^b, Derek Heathfield ^b

^a Department of Geography, Earth and Environmental Sciences, University of Northern British Columbia, Prince George, British Columbia V2N 4Z9, Canada

^b Hakai Institute, Campbell River, Quadra Island, British Columbia V9W 0B7, Canada

^c Department of Geography, University of Utah, Salt Lake City, UT 84112, USA

ARTICLE INFO

Edited by Menghua Wang

Keywords:

Imaging spectroscopy
Remote sensing
Snow
Glacier
Albedo
Topography

ABSTRACT

Observations of glacier albedo are sparse, despite being a first-order control on net solar radiation and melt rates. Recent and forthcoming airborne and satellite imaging spectrometer missions increase our ability to record changes in albedo over time and space but will require an understanding of uncertainties, especially in areas of rugged terrain. Some of these uncertainties arise from the timing of acquisition and resolution of digital elevation models (DEM) that are used for topographic correction. We use the fine-resolution data (2 m) from the Airborne Coastal Observatory (ACO), an imaging spectroscopy and lidar remote sensing platform, to quantify the expected error from other airborne and satellite scale platforms. First, we describe our retrieval workflow - the Imaging Spectroscopy Snow and Ice Algorithm (ISSIA) that yields spatial retrievals of broadband albedo (BBA), optical grain size, and radiative forcing by light absorbing particles (RF_{LAP}) using the coincident 2 m lidar DEM over mountain glaciers. We use two acquisitions over Place Glacier, British Columbia, Canada that represent typical spring and summer conditions as a baseline from which synthetic datasets were generated to represent data from coarser-scale imaging spectroscopy platforms. Each synthetic dataset was motivated by specific airborne and satellite platform scenarios and quantifies four sources of error: (1) DEM spatial resolution and elevation accuracy, (2) coincident vs non-coincident DEM collection, (3) imagery spatial resolution, and (4) spectral resolution. Use of a 30 m DEM introduced the most error in steep mountain terrain, which primarily increased error in the BBA and RF_{LAP} retrievals. The timing of DEM acquisition mattered most for high-resolution imagery and in areas surrounding the glacier toe where mass loss occurred more rapidly. Coarse-resolution imagery did not fully capture spatial variability in surface properties and topography, which lowered variance and increased overall errors. Coarsening of spectral resolution from 5 nm to 10 nm had minimal impact on surface property retrieval and associated errors were independent of DEM or imagery resolution. A simple energy analysis showed that surface albedo error, due to topographic correction with coarse and non-coincident DEMs, resulted in melt rate errors ranging from 6 to 20% for airborne and 11–20% for satellite scenarios.

1. Introduction

Snow and glaciers play a critical role for Earth's climate and terrestrial hydrology, but their extent is rapidly declining due to human-induced climate change (Hock et al., 2019). For seasonal snow, the surface albedo determines the shortwave energy balance and is the primary control on snowmelt timing (e.g., DeWalle and Rango, 2008;

Marks and Dozier, 1992). Many global glacier change studies consider temperature and precipitation as drivers of mass change (e.g., Hugonet et al., 2021; Rounce et al., 2023), although changes in albedo are also important (e.g., Dumont et al., 2012a). Commonly, albedo is parameterized in mass and energy balance models as a non-linear decay function (e.g. Oerlemans and Knap, 1998), but these models are error prone since they do not simulate many important factors responsible for

* Corresponding author at: Department of Geography, Earth and Environmental Sciences, University of Northern British Columbia, Prince George, British Columbia V2N 4Z9, Canada.

E-mail addresses: Donahue.Christopher@outlook.com (C.P. Donahue), Brian.Menounos@unbc.ca (B. Menounos).

physical properties that affect albedo (Abolafia-Rosenzweig et al., 2022; Minder et al., 2016). In the visible wavelengths albedo is controlled by deposition of light absorbing particles (LAPs) (Skiles et al., 2018), surface concentration of which vary seasonally due to weather and emissions from forest fire, land use change, and drought. In the near-infrared (NIR) wavelengths, albedo strongly depends on the grain size of snow and ice (Warren and Wiscombe, 1980). Albedo is highest after snowfall when grains are small and declines over time as grains grow and densify into firn and glacier ice. Variability and feedbacks, for example surface darkening leading to quicker grain growth, cannot be represented by a single decay function, which motivates the need to quantify spatial snow and ice albedo changes over time. Enhanced earth observations of snow and ice albedo would also allow us to improve radiation and energy balance in physically-based models that can be used to project likely changes of the cryosphere and melt rates under future climate.

Albedo, the ratio of total reflected to incoming solar radiation, cannot be directly observed by remote sensing instruments that only measure the portion of reflected light within their field of view, and must be derived. Workflows exist to derive snow albedo from satellite multispectral imagers, such as MODIS and Landsat (e.g., Bair et al., 2020; Painter et al., 2009). Because current multispectral imagers have few or no bands in the NIR where snow reflectance is most variable, snow albedo is modeled from retrieved snow properties. The low number of discontinuous bands and frequency of mixed pixels at coarse spatial resolution result in substantial retrieval uncertainties, especially in mountainous terrain. Imaging spectrometers, also referred to as hyperspectral sensors due to their high number of continuous bands, reduce retrieval uncertainty by leveraging the continuous spectral signature in each pixel. These data are most readily available from airborne imaging spectrometers, with added benefits of fine spatial resolution, low atmospheric interference, and high signal quality. Albedo from airborne imaging spectroscopy workflows have lower uncertainty relative to satellite platforms, although retrievals are sparse and infrequent due to the logistics and cost associated with aircraft data collection and have been primarily developed and assessed over seasonal snow (i.e., Painter et al., 2013; Seidel et al., 2016).

Recently, there have been several successful launches of satellite imaging spectrometers, which include the German Aerospace Center's DLR Earth Sensing Imaging Spectrometer (DESiS; Müller et al., 2016), the Italian Hyperspectral Precursor of the Application Mission (PRISMA; Cogliati et al., 2021), German Environmental Mapping and Analysis Program (EnMAP; Chabrillat et al., 2020), and NASA Earth Surface Mineral Dust Source Investigation (EMIT; Connelly et al., 2021). There are also several forthcoming missions, such as NASA Surface, Biology, and Geology (SBG; Cawse-Nicholson et al., 2021; Stavros et al., 2023), ESA Copernicus Hyperspectral Imaging Mission for the Environment (CHIME; Rast et al., 2021), and Planet's Tanager hyperspectral imager (<https://www.planet.com/products/hyperspectral>). With the growing number of orbital imaging spectrometers there is an opportunity to improve snow and ice albedo monitoring from space. The uncertainty from retrieval algorithms is less understood for satellite imaging spectroscopy which is typically coarser in spatial and spectral resolution relative to airborne sensors.

Retrievals of snow and ice surface properties from remote sensing are affected by topography, which influences measured spectral signature magnitude and shape (Carmon et al., 2023). These spectral distortions can be corrected by accounting for how topography impacts view and illumination angles, and results in shadowing, using a digital elevation model (DEM) (Richter and Schläpfer, 2011). At the airborne scale there are platforms that coincidentally collect imaging spectroscopy data and topographic data from lidar (e.g., Johnson et al., 2010; Painter et al., 2016), which is ideal. Standalone airborne imaging spectroscopy platforms and satellite imaging spectroscopy, however, need to use open-access DEMs, which are collected non-coincidentally, have low accuracy in differences between neighboring pixels, and are typically distributed at a coarse scale (e.g., 30 m) relative to mountain terrain

complexity (Dozier et al., 2022). There has not yet been a demonstration of topographic correction of satellite imaging spectroscopy over mountain snow or ice and limited studies have applied it at the airborne scale with non-coincident DEMs (Painter et al., 2013; Seidel et al., 2016).

As imaging spectroscopy becomes increasingly available, an assessment of error associated with coincident vs non-coincident DEM collection and spatial resolution, as well as imagery spatial and spectral resolution is required. Here, we present high resolution (2 m) retrievals of mountain snow and ice surface properties from the Airborne Coastal Observatory (ACO), an imaging spectrometer and scanning lidar platform. To conduct an error assessment, synthetic datasets were then generated from the baseline ACO data at various spatial and spectral resolutions to represent different airborne and satellite imaging spectrometer platform scenarios. Property retrieval error for each scenario was then quantified relative to the baseline.

The goal of our study is to:

- i. Describe the snow and ice surface property retrieval algorithm developed to process ACO imaging spectrometer data over western Canadian glaciers; and
- ii. Quantify the error in remotely sensed imaging spectroscopy retrievals due to DEM spatial resolution, accuracy, and timing, as well as imagery spatial and spectral resolution.

2. Background

2.1. Snow and ice albedo

Albedo, or bihemispherical reflectance (BHR), is the ratio of reflected radiant flux into the whole hemisphere to that of incoming hemispherical radiant flux (Schaeppman-Strub et al., 2006). The spectrally varying controls on snow and ice albedo are similar. In the visible wavelengths ice is transparent. For snow, incoming light is reflected (up to 99%) due to frequent scattering opportunities between grains. For ice, reflectance is lower (60–80%) than snow because scattering at enclosed air bubbles are less frequent. When LAPs, such as dust and black carbon, are deposited on snow or ice surface albedo in the visible portion of the electromagnetic spectrum decreases. During melt, many LAPs are not entrained in the runoff and will combine at the snow surface to accelerate albedo decay and melt rates. These conditions can provide the nutrients and surface water needed to support algae blooms, which additionally contribute to surface darkening (Hotaling et al., 2021). On glaciers LAPs can accumulate on the bare ice surface for multiple years, which compounds glacier darkening (Oerlemans et al., 2009). The impact of LAPs is commonly quantified using the radiative forcing; the increase in absorbed solar radiation due to the surface darkening (Skiles et al., 2018).

Albedo in the near-infrared (NIR) wavelengths is controlled by the snow and ice grain size. As the ice grain size increases, the path length of ice also increases, which increases light absorption and reduces NIR albedo. Generally, fresh snowfall deposits small-grained snow at the surface and due to metamorphism, the grains grow over time. Rates of growth are faster under temperature gradients (Calonne et al., 2014), at warmer air temperatures (Kaempfer and Schneebeli, 2007), in the presence of liquid water (Donahue et al., 2021), and surface darkening by LAPs (Skiles and Painter, 2019). In glaciated areas where snow is perennial, the grain growth process continues throughout the firnification and glaciation processes. As previously mentioned, there is a point at which ice becomes more continuous than air and scattering occurs at air bubble interfaces rather than ice particle surfaces (Gardner and Sharp, 2010).

Over the last several decades a significant body of work has quantified the optical properties of snow and ice and developed radiative transfer models that accurately simulate measured spectral reflectance. The traditional methodology for simulating snow reflectance is done by representing snow as a collection of ice spheres with a known radius,

referred to as the optical or effective grain radius (Warren and Wiscombe, 1980). This approach was followed, for example, by Nolin and Dozier (2000) who used single scattering optical properties from Mie theory to simulate multiple scattering and reflectance with the multi-stream Discrete Ordinates Radiative Transfer Program (DISORT; Stamnes et al., 1988). Snow spectra were simulated for a range of ice sphere radii, and then related to measured snow reflectance from airborne imaging spectroscopy to map snow grain size, an approach which was adopted by subsequent studies for field and imaging spectroscopy retrievals (Donahue et al., 2021; Painter et al., 2007, 2013; Skiles and Painter, 2017). However, snow on the ground is made up of irregular shaped grains and the optical properties are controlled by both the size and shape of the particles (Mishchenko et al., 1999). As an example, spherical particles scatter light in the forward direction more strongly than other particle shapes, which can result in underestimation of grain size from optical instruments (Fair et al., 2022; Jin et al., 2008). Snow also becomes more backscattering as surface roughness increases, for example with the formation of sun cups during ablation, although without observations of surface evolution this can be challenging to account for in remote sensing retrievals (Bair et al., 2022; Larue et al., 2020). More recent models represent snow grains with various shapes, including fractals, spheroids, and hexagonal plates and also simplify radiative transfer calculations into two-stream or analytic approaches (Flanner et al., 2021; Kokhanovsky and Zege, 2004; Libois et al., 2013). These radiative transfer models are commonly used as a forward model to invert imaging spectroscopy measurements to physical snow properties.

2.2. Snow and ice property retrieval from imaging spectroscopy

Imaging spectrometers measure spectral radiance within their field of view, which is converted to top of atmosphere reflectance and then at-surface reflectance using an atmospheric correction workflow. The spectral reflectance signature can then be leveraged to derive snow properties, by relating the measured to modeled spectra with known characteristics, and spectral albedo, by accounting for the local geometry between the illumination and viewing angles. For seasonal snow, retrievals of optical grain size (Nolin and Dozier, 2000), surface liquid water content (Green et al., 2006), surface darkening by LAPs, and albedo (Painter et al., 2013; Seidel et al., 2016) have been demonstrated using this approach from the NASA Jet Propulsion Laboratory's Airborne Visible and Infrared Imaging Spectrometer (AVIRIS). Algorithms developed to extract these properties have been adapted to commercial imaging spectrometers on airborne (Painter et al., 2016), UAV (Skiles et al., 2023), and ground based platforms (Donahue et al., 2022). An alternative approach is to retrieve atmospheric (water vapor) and surface parameters (grain size, water fraction, LAP concentrations) simultaneously using statistical correlations between measured and simulated reflectance, which has been demonstrated using AVIRIS data over a portion of the Greenland Ice Sheet (Bohn et al., 2021). With the recent launch of the satellite imaging spectrometer PRISMA, snow and ice property retrievals have also been demonstrated from space over the Greenland and Antarctic ice sheets (Bohn et al., 2022; Kokhanovsky et al., 2022), but these methodologies have yet to include treatment of topography and therefore would not be suitable for mountain snow and ice. A gap in this previous work is airborne imaging spectroscopy for snow and ice surface properties over topographically complex terrain such as Earth's mountain environments.

2.3. Topographic correction

Retrieval of snow and ice properties from imaging spectroscopy depends on the absolute magnitude of reflectance as well as the shape of the reflectance spectra. Over flat terrain, atmospheric conditions generally lack spatial variability and retrievals are simple. In mountainous terrain, however, a DEM is needed to calculate pixel-wise aspect,

slope, sky view factor, and local horizons that are used to define the solar illumination geometry and topographically correct at-sensor radiance. The spatial resolution and timing of DEM acquisition, relative to the imaging spectroscopy acquisition, introduce error and uncertainty to the solar illumination geometry (Dozier et al., 2022). Deep snow, for example, can smooth the topography making the solar illumination geometry different from what would be calculated with a DEM acquired during snow-free conditions. Similarly, glacier flow and mass change can alter surface topography over small time scales. With the increasing number of satellite imaging spectrometers, topographic corrections of these data will predominately rely on coarse (30 m), relative to mountain terrain, globally available DEMs. Dozier et al. (2022) quantified the error and uncertainty in solar illumination geometry related to using these types of DEMs, but how that propagates to the error in retrieved physical properties of snow and ice surface property retrievals remains uncertain.

3. Study site and data description

3.1. Study site

We present data collected over Place Glacier (50.417 N, -122.601 W), located in the Coast Mountain Range of British Columbia (Fig. 1a). The 3.02 km² glacier is one of Canada's benchmark glaciers, being monitored for mass change since 1965 (Mukherjee et al., 2022). The maximum and minimum elevation of Place Glacier respectively is 2054 and 1850 m above sea level (m ASL), and the glacier flows north to northeast within topographically complex terrain (Fig. 1b).

3.2. Airborne Coastal Observatory (ACO)

The ACO is an aerial remote sensing platform with a dedicated lidar, imaging spectrometer, and high-resolution aerial cameras that acquires data over glaciers and snow-covered terrain in Western Canada. The instrumentation is housed in a Piper Navajo aircraft with nadir instrumentation viewing ports through the floor. Data fusion of lidar altimetry and imaging spectroscopy is gaining popularity as a detailed and flexible way to study changing landscapes. Lidar and imaging spectrometer platforms include the National Science Foundation's National Ecological Observatory Network (NEON), mapping long term ecological change (Johnson et al., 2010), and the Carnegie Airborne Observatory (CAO) (Asner et al., 2007), mapping sensitive ecosystems like rainforests and coral reefs in support of conservation. The NASA Airborne Snow Observatory (ASO) program (Painter et al., 2016) applied this concept to snow hydrology, acquiring time series of seasonal snow depth in the western United States. The ACO uses a similar data fusion approach, however a primary focus of the ACO is to quantify glacier change in Western Canada.

The analysis presented here was carried out for two ACO acquisitions that captured contrasting snow and glacier ice conditions. The first flight occurred on 16 April 2021, hereafter referred to as spring flight, during which the entire glacier and surrounding mountains were covered in snow. The second flight was on 7 August 2022, hereafter referred to as summer flight, where the accumulation zone of the glacier was still snow-covered but bare ice was exposed at the glacier toe, and the surrounding mountains were snow free. The skies were clear and data acquisition took place within one hour of solar noon for both flights. The solar zenith angle was 40° and 38° respectively for the spring and summer flights. The entire glacier was captured in six south to north flight lines with 50% overlap (200% coverage).

3.2.1. ACO instrumentation

The ACO imaging spectrometer is a Specim Fenix which measures reflected solar radiation from Earth's surface in the visible to shortwave infrared (SWIR) with a high signal-to-noise ratio (SNR; 600–1000). The instrument is comprised of two sensors with the same optics that have a

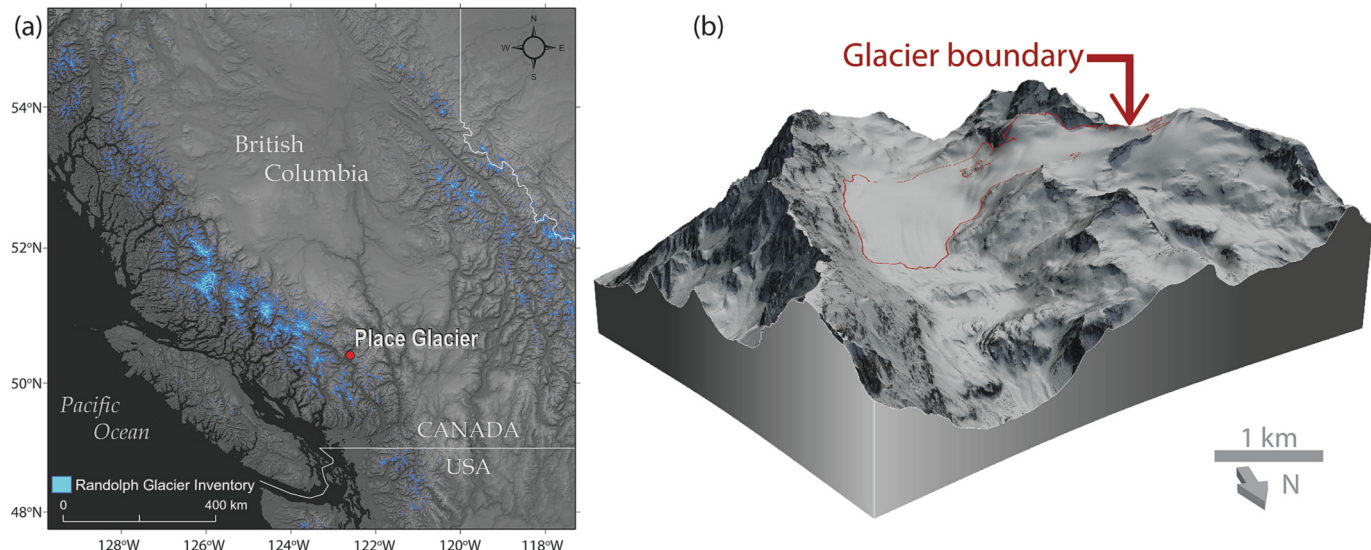


Fig. 1. (a) Map showing the location of Place Glacier in the Coast Mountains of British Columbia, Canada. Light blue polygons are glaciers from the Randolph Glacier Inventory - Version 6.0 (RGI Consortium, 2017). (b) 3-dimensional visualization of Place Glacier on 16 April 2021 produced from Airborne Coastal Observatory data. The glacier boundary is outlined in red. (For interpretation of the references to colour in this figure legend, the reader is referred to the web version of this article.)

32.3° field of view. The visible to near infrared (VNIR) sensor has a spectral range of 380 to 970 nm with a spectral resolution of 3.5 nm and the SWIR sensor has a range of 970 to 2500 nm with a spectral resolution of 12 nm. The instrument is operated in spectral binning mode, acquiring imagery with 451 bands across the full spectral range with an average spectral sampling interval of 3.4 nm in VNIR range and 5.7 nm in SWIR range. The plane flew at a median altitude of 1400 m above ground level (m AGL), allowing for the imagery to be processed to 2 m spatial resolution.

Our laser scanner is a Riegl LMS-Q 780 that emits laser pulses in the NIR at a wavelength of 1064 nm; the time of flight of each returned laser pulse was used to map surface elevations. The point cloud was binned to a 2 m gridded DEM, co-registered with the imaging spectrometer imagery, and used to calculate slope, aspect, and sky view factor, which are required for topographic correction of imaging spectroscopy data. Additionally, the DEM was used to produce a binary shadow map based on the local horizon, and areas shadowed by surrounding terrain were masked (small fraction of area primarily during spring acquisitions). The horizontal and vertical positional uncertainties are ±0.15 m, which was quantified from repeat surveys over stable terrain (Pelto et al., 2019).

The aircraft is also equipped with dual Phase One 100 MP aerial cameras (RGB + NIR). Continuous photographs are taken during the flight acquisition and are post-processed to georectified orthomosaics. The imagery is finer resolution (0.15 m) than a true colour composite from the imaging spectrometer, which is useful for visualization and assessment of ground conditions at time of flight. An example of this data was used to produce the 3D visualization in Fig. 1b.

4. Imaging spectrometer snow and ice algorithm

The snow and ice surface property retrievals from the imaging spectrometer include broadband albedo (BBA), optical grain radius, hereafter referred to as grain size, and radiative forcing by light absorbing particles (RF_{LAP}). The retrieval methodology largely follows the algorithm suite referred to as Imaging Spectrometer-Snow Albedo and Radiative Forcing (IS-SnARF) (Painter et al., 2013). We briefly describe the retrieval method and discuss key modifications to the algorithm implemented in the current study. The modifications increase the suitability for retrieving properties over large-grained snow and bare ice, which are typical for alpine glaciers in Western Canada throughout the spring, summer, and autumn. We herein refer to our approach as

Imaging Spectrometer Snow and Ice Algorithm (ISSIA). The reader is directed to Painter et al. (2013) for a detailed description of the algorithm, as well as other references throughout this section for details on the legacy of snow and ice retrievals.

4.1. Hemispherical-directional reflectance factor

In order to retrieve optical properties, the surface hemispherical-directional reflectance factor (HDRF) needs to be calculated from the measured radiance at the sensor (L_{sensor}) (Schaeppman-Strub et al., 2006):

$$HDRF_{sfc}^{obs} = \frac{\pi(L_{sensor} - L_{atm})}{TE_g} \quad (1)$$

Where L_{atm} is the radiance component due to scattering and absorption in the atmosphere, T is the atmospheric transmission, and E_g is the total (direct + diffuse) solar irradiance at the ground. Each of these factors, excluding L_{sensor} , were simulated using the Atmospheric and Topographic Correction for Airborne Imagery (ATCOR-4) software (Richter and Schlüfer, 2011) using the rural aerosol model, which was selected due to the high elevation of the glacier and distance from urban centers. The rugged terrain program within ATCOR-4 accounts for the influence of topography by using a DEM to calculate a pixelwise slope, aspect, and sky-view factor. The 2 m ACO imagery was processed using the coincidentally acquired 2 m ACO DEM; we herein refer to these datasets as our ‘baseline dataset’ that we used to produce and assess synthetic remote sensing scenarios, described in Section 5. The synthetic remote sensing scenarios were output from ATCOR-4 at 30 m resolution and processed with either a coarser coincident ACO DEM, resampled from 2 m to 30 m, or a non-coincidentally collected Copernicus global 30 m DEM (GLO-30; European Space Agency, 2021) reprojected to WGS-84 to match the ACO DEM.

4.2. Snow and ice extent

We used the normalized difference snow index (NDSI) (Dozier, 1989; Dozier and Marks, 1987; Hall et al., 1995) to delineate snow and ice covered pixels from other land surface types.

$$NDSI = \frac{HDRF_{\lambda=600\text{ nm}} - HDRF_{\lambda=1500\text{ nm}}}{HDRF_{\lambda=600\text{ nm}} + HDRF_{\lambda=1500\text{ nm}}} \quad (2)$$

This method leverages the large difference in reflectance between

wavelengths (λ) in the visible and shortwave infrared regions of the spectrum. A threshold of NDSI >0.87 was used because it accurately captured snow and glacier ice based on visual inspection relative to ortho images acquired during the same flight. Pixels that contained very dark glacier ice, or perhaps debris, were excluded in the summer flight due to the difference in visible and NIR reflectance being too low. The quantitative retrievals were performed only in pixels that were identified using NDSI because they are assumed to be fully snow or ice covered and not mixed with any other land surface type (i.e., rocks or vegetation).

4.3. Grain size

Our grain size retrieval uses a forward modeling approach where the spectral $HDRF_{sfc}^{obs}$ is fit to modeled spectral hemispherical-directional reflectance ($HDRF_{sfc}^{mdl}$) from radiative transfer modeling. The asymptotic radiative transfer (ART) model (Kokhanovsky and Zege, 2004) was used to generate a lookup table of simulated reflectance spectra of clean snow. The primary motivation for choosing ART was because it uses geometric optics which is a more suitable modeling approach for retrieving large snow grain sizes, such as those found in perennial snow cover or over bare glacier ice. A secondary motivation was that ART models snow as a collection of close-packed fractal ice grains which is a closer representation to the complex and irregular shape of snow grains. Mie scattering theory (Bohren and Huffman, 1998), used in IS-SnARF, models snow as a collection of spherical grains, but this approach underestimates grain size based on theoretical arguments (Kokhanovsky and Zege, 2004) and from observations (Donahue et al., 2021; Gergely et al., 2013).

Our grain size retrieval also deviates from IS-SnARF by adopting the method presented in (Clark and Roush, 1984) which related grain size to the depth of the ice absorption feature centered at 1030 nm. This work showed that the apparent continuum, the reflectance in the absence of the absorption feature, could be used as a reference point from which a continuum normalized band depth could be calculated. Normalization translates absolute reflectance magnitude into a descriptor of feature shape, which scales, inversely and nonlinearly, with grain size. This method was highlighted as being sensitive to noise by Nolin and Dozier, 2000, which presented an alternative method using the continuum-removed area of the ice absorption feature as the fitting parameter. The Nolin-Dozier approach leverages the shape and depth of the absorption feature making it less sensitive to noise relative to the single band used to calculate depth. This approach is only suitable for dry snow conditions, however, because the left shoulder of the absorption feature shifts to smaller wavelengths with the presence of water, resulting in a negative grain size bias (Donahue et al., 2022). Recognizing potential issues with liquid water, Painter et al. (2013) used a modified Nolin-Dozier approach, using only the right shoulder of the absorption feature which is less affected by liquid water. This approach, though, is more sensitive to the absolute magnitude of the reflectance spectrum. To address the limitations in these previous methods, we return to the continuum-removed depth of the ice absorption feature as the fitting parameter (Fig. 2). The presence of liquid water can shift the location of the minimum band in the absorption feature, but it does not have a significant impact on the depth itself. Modern imaging spectrometers, like that on the ACO, have high spectral resolution and SNR eliminating the concerns originally raised by Nolin and Dozier (2000).

4.4. Albedo

To calculate albedo (α), the measured HDRF must be converted to BHF based on the spectral anisotropy factor (c) because snow preferentially scatters light in the forward direction (Dumont et al., 2010). We note that this assumes snow is predominantly forward scattering and neglects decreasing forward scattering with increasing surface

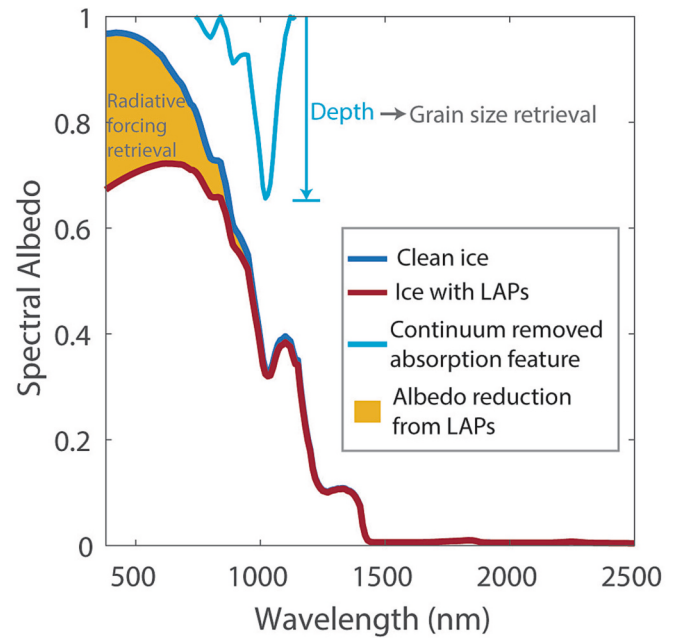


Fig. 2. Example of the optical grain size and radiative forcing by LAPs retrieval. Albedo spectra were simulated using the Asymptotic Radiative Transfer model. The grain radius for both spectra is 2 mm and the soot concentration for the red spectra is 1000 ng/g. (For interpretation of the references to colour in this figure legend, the reader is referred to the web version of this article.)

roughness due to the challenges in characterization. The anisotropy factor is based on simulated spectral albedo and HDRF at varying incident, viewing, and azimuth angles:

$$c_{\theta_0, \theta_v, \phi_0 - \phi_v; r; \lambda} = \frac{\alpha_{sfc}^{mdl}(r; \lambda)}{HDRF_{sfc}^{mdl}(\theta_0, \theta_v, \phi_0 - \phi_v; r; \lambda)} \quad (3)$$

Where r is the grain size (radius), θ_0 is the local solar zenith angle, θ_v is the local viewing angle, and $\phi_0 - \phi_v$ is the relative azimuth angle between the local solar and viewing angles. These local angles account for the terrain slope and aspect, but for simplicity, we avoid subscripts denoting these terms in our notation. The measured HDRF was then converted to α :

$$\alpha_{sfc}^{obs}(r; \lambda) = HDRF_{sfc}^{obs}(\theta_0, \theta_v, \phi_0 - \phi_v; r; \lambda)^* c_{\theta_0, \theta_v, \phi_0 - \phi_v; r; \lambda} \quad (4)$$

The broadband albedo can then be calculated by spectrally integrating Eq. (4) with the modeled direct and diffuse spectral irradiance (E_{sfc}^{mdl}) at the surface, which is output as a total global irradiance from ATCOR-4:

$$\alpha_{sfc}^{obs}(r) = \frac{\int_{\lambda=0.38 \mu m}^{2.5 \mu m} E_{sfc}^{mdl}(\lambda; \theta_0) * \alpha_{sfc}^{obs}(r; \lambda) d\lambda}{\int_{\lambda=0.38 \mu m}^{2.5 \mu m} E_{sfc}^{mdl}(\lambda; \theta_0) d\lambda} \quad (5)$$

4.5. Radiative forcing by light-absorbing particles

The radiative forcing by LAPs (RF_{LAP}) is calculated by taking the difference between the modeled clean snow/ice albedo for the retrieved grain size and the observed albedo across the visible wavelengths. The reduction in albedo is multiplied by E_{sfc}^{mdl} to determine the instantaneous radiative forcing in terms of $W m^{-2}$:

$$RF_{LAP} = \int_{\lambda=0.38 \mu m}^{1.0 \mu m} E_{sfc}^{mdl}(\lambda; \theta_0) * \left(\alpha_{sfc}^{mdl-clean}(r; \lambda) - \alpha_{sfc}^{obs}(r; \lambda) \right) d\lambda \quad (6)$$

This method assumes that LAPs have a small impact in the NIR beyond 1 μm (Warren and Wiscombe, 1980) and the grain size retrieval

Table 1
Synthetic dataset scenarios used in the analysis.

Scenario	Spatial Resolution		DEM source/timing	Spectral resolution
	Imaging spectroscopy	DEM		
Airborne				
A1 _{5/10 nm}	2 m	2 m	ACO / coincident	5 nm / 10 nm
A2 _{5/10 nm}	2 m	30 m	ACO / coincident	5 nm / 10 nm
A3 _{5/10 nm}	2 m	30 m	Copernicus / non-coincident	5 nm / 10 nm
Satellite				
S1 _{5/10 nm}	30 m	30 m	ACO / coincident	5 nm / 10 nm
S2 _{5/10 nm}	30 m	30 m	Copernicus / non-coincident	5 nm / 10 nm
S3 _{5/10 nm}	30 m	N/A	N/A	5 nm / 10 nm

is not impacted (Fig. 2).

5. Synthetic airborne and satellite imaging spectroscopy datasets

For our study, the retrievals from the coincidentally collected ACO 2 m imaging spectroscopy imagery and 2 m DEM are assumed to be truth and are used as a baseline from which we evaluate the other synthetic datasets. The dataset (Table 1) includes specific airborne and satellite platform scenarios and quantifies four sources of uncertainty: (1) imaging spectroscopy spatial resolution, (2) DEM spatial resolution and elevation accuracy, (3) coincident vs non-coincident DEM collection, and (4) spectral resolution. We divided the scenarios into three airborne cases (A1-A3) and three satellite cases (S1-S3), each processed at 5 nm and 10 nm spectral resolution, which we denote with subscripts. The total number of individual scenarios is 12, including the baseline (A1_{5nm}).

For imaging spectroscopy retrievals in mountainous terrain, a DEM is used to account for the local view and illumination angle, sky view factor, and shadowing. Most airborne imaging spectrometers platforms, such as AVIRIS-NG, do not collect a coincident DEM and must rely on static non-coincident globally available DEMs (typically 30 m spatial resolution). This is the motivation for scenarios A2 and A3, where we compare results from 2 m resolution imaging spectroscopy data processed with a 30 m coincidentally collected ACO DEM (A2) and a non-coincident Copernicus global DEM (A3).

Similarly, satellite imaging spectrometers must also rely on globally available DEMs, which is the scenario that motivates S1 and S2. These scenarios use the same 30 m ACO and Copernicus DEMs as in the airborne cases, but the spatial resolution of the imaging spectroscopy data was processed by ATCOR-4 software package at 30 m resolution. This mimics the spatial resolution of current and planned satellite imaging spectrometers (e.g., PRISMA and Tanager). To quantify the importance for topographic correction in mountain terrain, S3 was processed assuming flat terrain using the flat terrain atmospheric correction algorithm in the ATCOR-4 software package and running the ISSIA retrieval algorithm with the pixel-wise slope and aspect set to zero.

Current satellite imaging spectrometers collect data using 10 nm band spacing (e.g., PRISMA), and future satellites such as Planets Tanager will collect at 5 nm. Similarly, airborne spectrometers are typically manufactured with 5 or 10 nm band spacing, with the finer spectral resolution instrument being higher cost. To determine the impact of spectral resolution on snow and ice retrievals, each of the scenarios were processed at 5 nm and 10 nm. These datasets were generated by simply binning the reflectance spectra in each scenario. The spectral resolution for each scenario is denoted as a subscript (e.g., S1_{10 nm}).

To compare retrievals across scenarios that ranged from 2 m to 30 m spatial resolution, each of the retrieval products were reprojected to an intermediate spatial scale. Following the methodology used in Dozier et al. (2022), the intermediate scale was chosen using the approximate geometric mean of the two resolutions (2 m and 30 m), which is 8 m. The retrievals from all the scenarios were reprojected to the common 8 m grid using bilinear interpolation. For this approach, the dataset

resampled from the finer scale data is the reference, and the error being quantified is for the dataset that is resampled from the coarser DEM (Dozier et al., 2022). Pixels that were coarsened adjacent to null values were excluded to reduce errors from edge effects.

6. Results

First, we present the topography over the study site and compare the ACO and Copernicus DEMs (section 6.1). Then we describe the baseline ACO imaging spectroscopy retrievals (A1_{5nm}) and orthomosaic images for the two flight dates that we used as the reference from which the other scenarios are evaluated against (section 6.2). Sections 6.3 and 6.4 present results for the airborne and satellite scale scenarios at 5 nm resolution. Section 6.5 focuses on spectral resolution, comparing the 5 nm retrievals to the coarse spectral resolution (10 nm) for airborne and satellite scenarios. The combined results for the airborne and satellite scenarios are presented in Taylor plots (Taylor, 2001), which graphically displays the root-mean-squared (RMS) error, standard deviation, and Pearson correlation for each scenario compared to the baseline retrievals. The statistics used in the Taylor plots can be found in the supplementary materials (Table S1).

6.1. Digital elevation model comparison

The accuracy and resolution of a DEM used for topographic correction of imaging spectroscopy data in rugged terrain is a key contributor to retrieval error. The digital terrain (2 m) within the study site acquired by the ACO on 16 April 2021 displays the topographic complexity of the study area (Fig. 3a). The glaciated area has relatively low terrain complexities, while the surrounding mountains have steep peaks. This complexity is also revealed in the aspect-slope map (Fig. 3b), where the glacier is predominantly north to northeast facing and has small slopes compared to the varied, non-glacierized terrain. Although DEM, slope, and aspect maps are only presented for the spring flight using ACO data, they are generally representative of the summer flight and the Copernicus global DEM.

We reprojected the 2 m DEM from ACO and the 1 arc-second (~30 m) Copernicus DEM (Fig. 4) to a common intermediate resolution of 8 m for comparison. The analysis only considered pixels that were snow- or ice-covered based on the NDSI. The elevation of the Copernicus DEM had a positive bias compared to the ACO DEM, but the linear regression plots (Fig. 4a-b) show a good fit ($R^2 = 0.99$). The largest biases are at low elevation where the glacier lost mass and thinned between the date of the Copernicus DEM (ca. 2013) and the ACO surveys. Although elevations of both DEMs strongly covary, small errors in elevation propagate to larger errors in the aspect and slope derivative products (Fig. 4c-f), which are critical elements for topographic correction and the ISSIA retrieval algorithm. Note that in Fig. 4e-f, differences in aspect exceeding 180 degrees were angle wrapped to account for the discontinuity at North. The spring flight has overall more slope and aspect error compared to the summer flight because there were more pixels included in snow covered steep terrain (see section 6.2). This analysis indicates that a coincidentally collected DEM is more important for

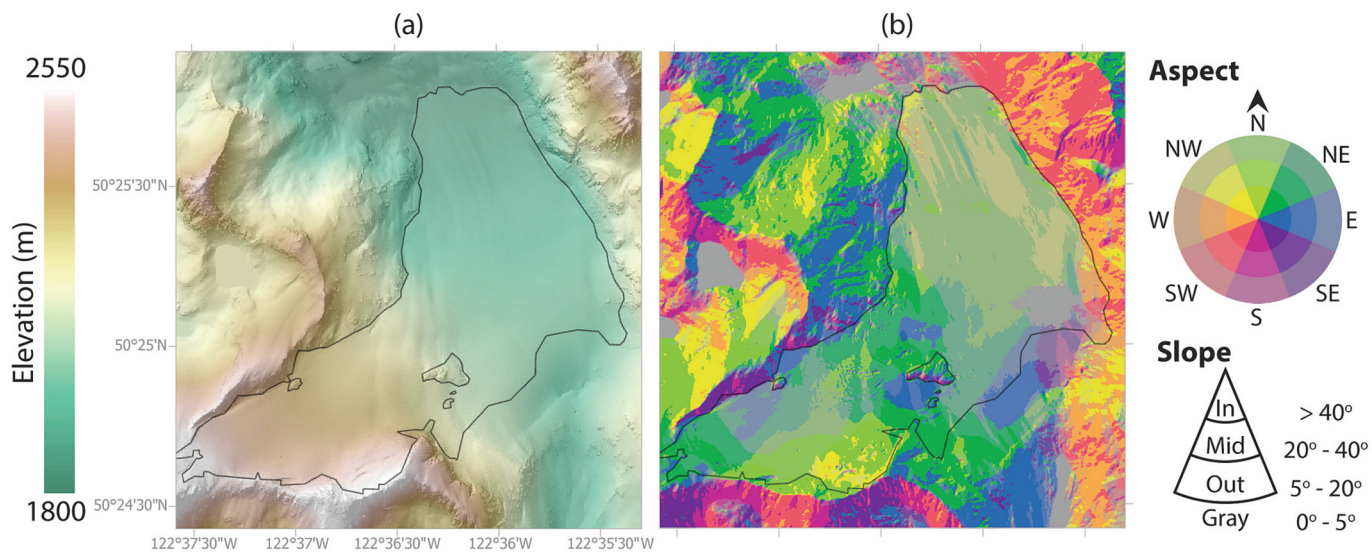


Fig. 3. Place Glacier topography measured from the Airborne Coastal Observatory on 16 April 2021. (a) Map of digital elevation model (2 m) with glacier boundary outlined in black. (b) Aspect-slope map where the colour indicates direction of aspect and saturation indicates steepness of slope; saturation levels correspond to the categories defined in the slope ‘pie’ legend.

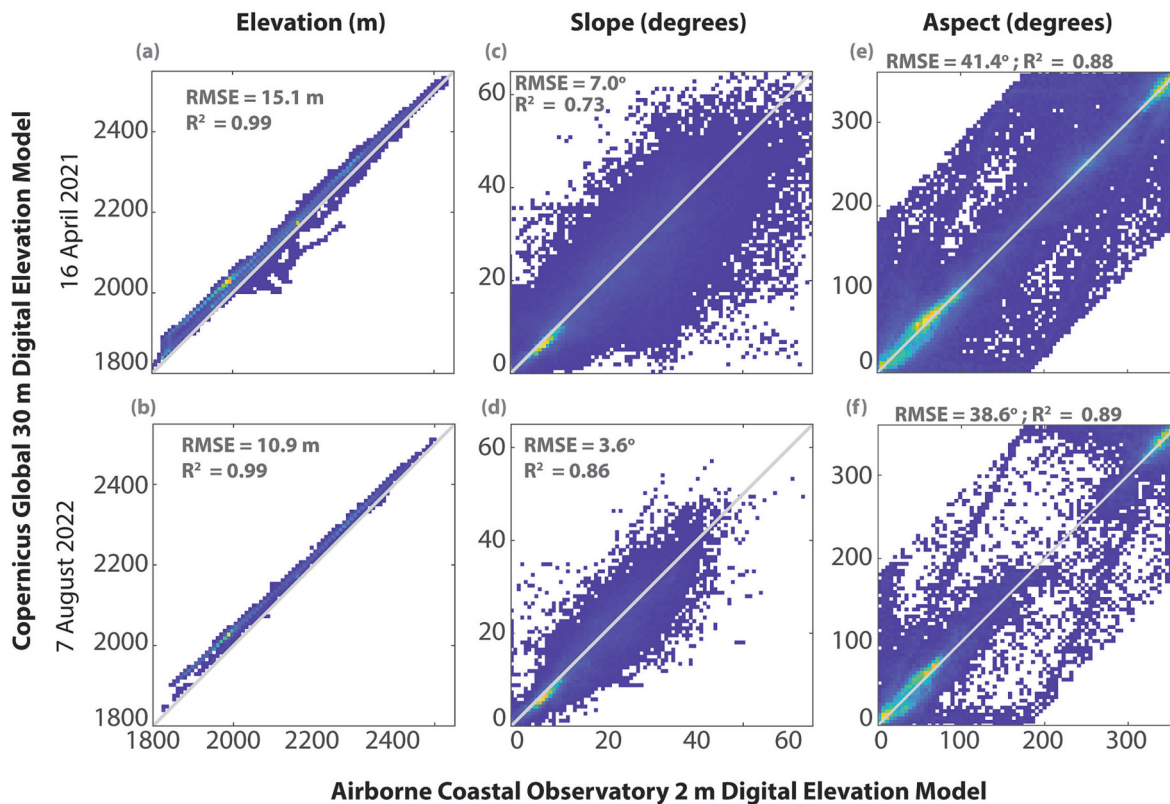


Fig. 4. Comparison of the Airborne Coastal Observatory 2 m DEM and Copernicus global 30 m DEM for each of the two flights. For comparison, both DEMs were resampled to an intermediate scale of 8 m and only pixels that contained snow or ice retrievals were included. The colour scale indicates the density of points with yellow being high density and the gray line represents the 1:1 line. (For interpretation of the references to colour in this figure legend, the reader is referred to the web version of this article.)

imaging spectroscopy measurements during the winter and spring and less important in the summer when snow cover is limited to less complex glaciated terrain.

6.2. Baseline ACO retrievals

The baseline 2 m ACO retrievals (Fig. 5) show the glacier and surrounding mountains were snow-covered during the spring acquisition, whereas snow was limited to the upper elevations of the glacier during the summer flight. The mean broadband albedo (BBA) was higher in the

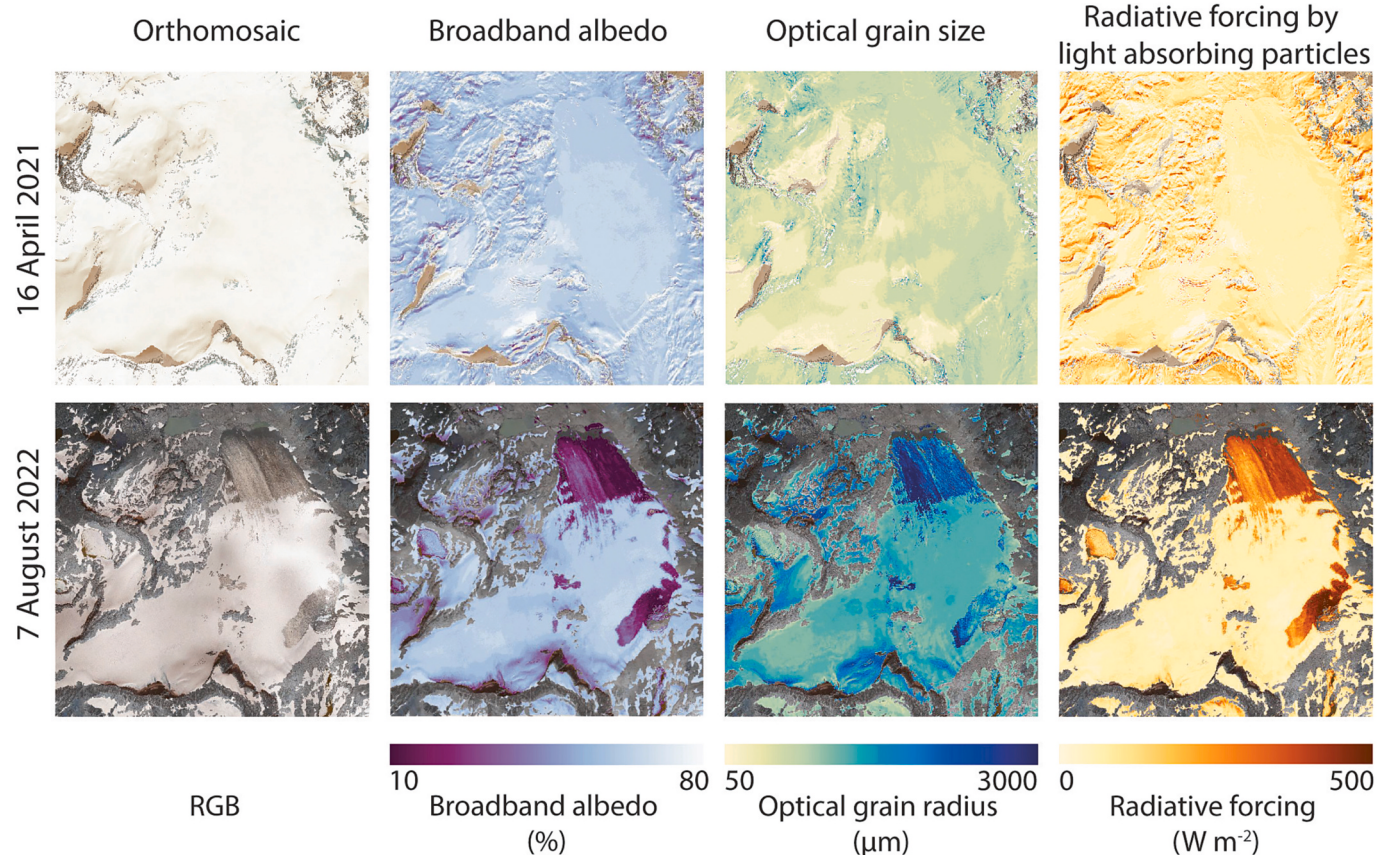


Fig. 5. Orthomosaic and imaging spectroscopy retrievals over Place Glacier, British Columbia, Canada from the Airborne Coastal Observatory on 16 April 2021 and 7 August 2022. These retrievals are used as the reference from which all other resolutions are compared against.

spring (61.0%) compared to the summer (52.1%). This was attributed to the smaller average grain size ($590 \mu\text{m}$) and lower RF_{LAP} (95.6 W m^{-2}) in the spring, whereas the summer flight had larger average grain size ($1416 \mu\text{m}$) and higher RF_{LAP} (116.8 W m^{-2}), which was in part due to the exposed ice at the glacier toe.

6.3. Airborne scenarios

The airborne scenarios, processed with the 30 m DEM, generally had higher error in the spring flight due to the retrievals over the snow-covered surrounding mountains, whereas the summer flight had lower error due to the retrievals being limited to snow and ice over less complex glaciated terrain. The spring flight using the coincident 30 m ACO DEM ($\text{A2}_{5\text{nm}}$) yielded a positive BBA bias (1.3%) that was a result of a positive grain size bias ($48 \mu\text{m}$) and negative radiative forcing bias (11.2 W m^{-2}). Interestingly, the grain size and RF_{LAP} biases offset each other to reduce error in BBA, but the RF_{LAP} error dominates the overall error in BBA. Relative to the baseline retrieval, the RF_{LAP} correlation (0.45) was low, while the grain size correlation remained relatively high (0.90), indicating that the RF_{LAP} retrieval is more susceptible to error from a coarsened DEM. In contrast, the late summer flight yielded a slight negative BBA bias (0.4%) that was a result of a small bias in grain size ($5 \mu\text{m}$) and RF_{LAP} (2.0 W m^{-2}). The grain size RMSE was higher for the summer flight, but this did not have a large effect on BBA error relative to the RMSE for the spring flight. This phenomenon is due to the non-linear inverse BBA-grain size relationship; grain size change for small particle sizes has a larger impact on BBA than grain size changes at large particle sizes. The correlation remained high for all the retrievals (>0.95) indicating that error was greatest in mountainous snow-covered terrain compared to less complex glaciated terrain when using a coarse DEM.

The errors due to using a non-coincident DEM are quantified by comparing the results from scenarios $\text{A2}_{5\text{nm}}$ and $\text{A3}_{5\text{nm}}$ (Fig. 6). For both flights, the RMSE increased across all retrievals, and the correlation decreased. The relative magnitude of RMSE increase were similar between flight dates and were approximately 1% for BBA, 25 μm for grain size, and 10 W m^{-2} for RF_{LAP} . Correlation weakened most for the spring acquisition, most notably for RF_{LAP} and BBA (Fig. 6). The largest differences in BBA were at the glacier toe, in the steep terrain adjacent to the glacier, and at the edges of the glacier. In the spring flight, it is apparent that part of the glacier toe had disappeared in the time between the Copernicus and ACO DEM acquisitions and that the terrain in this area was misrepresented in $\text{A3}_{5\text{nm}}$. This topography error caused a positive BBA error surrounding the glacier toe. In contrast, changes in non-coincident DEMs were minor for summer due to reduced coverage of snow in complex terrain. The contrast in correlation magnitude between the two flight dates can be seen in the BBA difference maps (Fig. 7). Grain size and RF_{LAP} difference maps between the baseline ACO retrievals and each airborne and satellite scenario are presented in Supplementary Figs. 1 and 2, respectively.

6.4. Satellite scenarios

For the airborne scenarios (A2 and A3) the error could be directly attributed to the change from a fine resolution to coarser resolution DEM, and correspondingly, the additional error in the satellite scenarios could be attributed to the coarser scale imagery. The 30 m resolution imagery smooths out the variability, which is apparent in lower standard deviations across the different surface property retrievals (Fig. 6). Note that the coarser resolution reduced the spatial extent of snow and ice (Fig. 7 relative to Fig. 8) because more of the pixels were mixed at 30 m, but that only pixels containing snow and ice were used to quantify

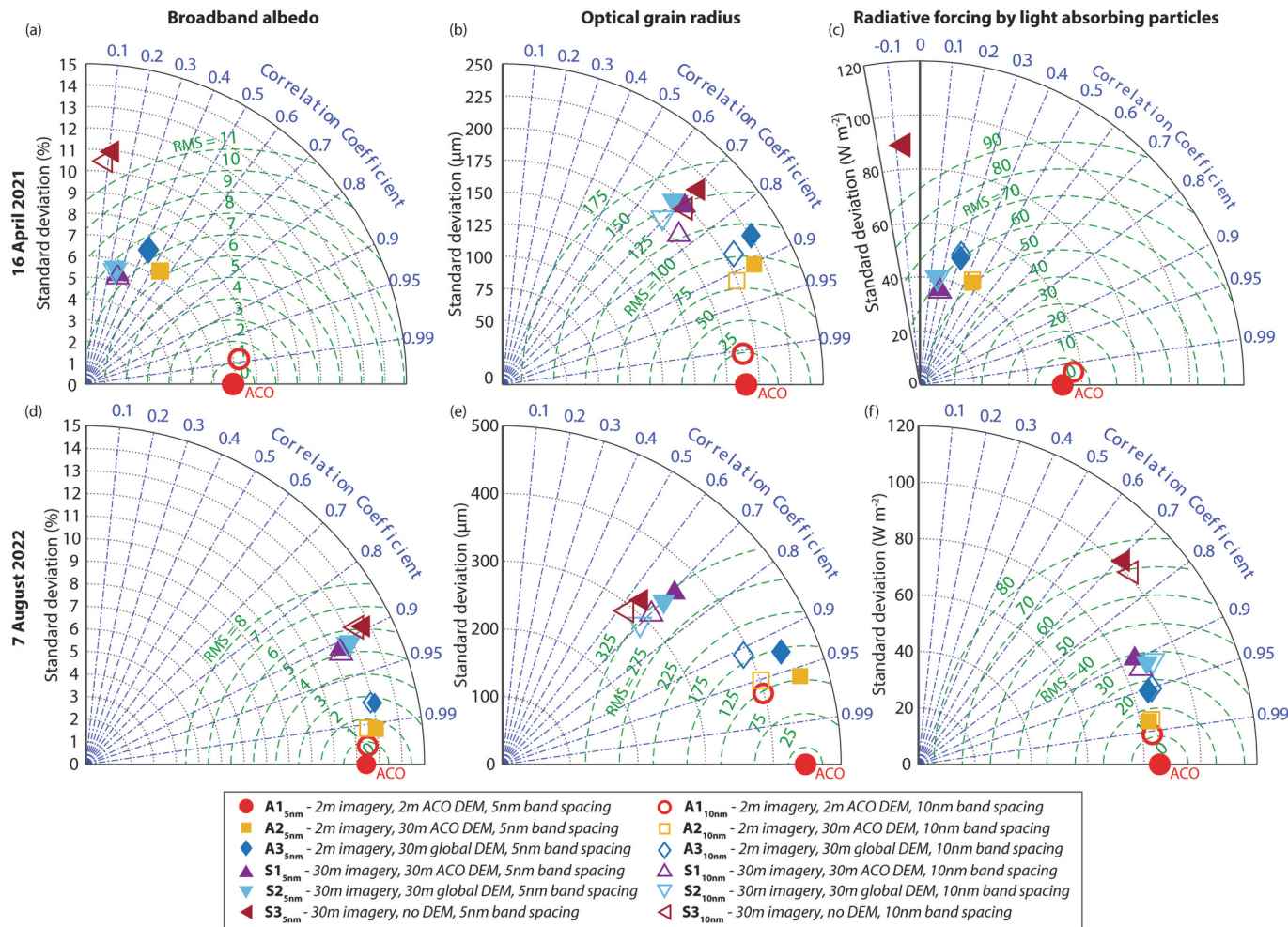


Fig. 6. Taylor plots for the evaluation of broadband albedo, optical grain size, and radiative forcing by light absorbing impurities for each synthetic dataset. All datasets are compared against the reference Airborne Coastal Observatory retrieval (A1_{5nm}; solid red circle). (For interpretation of the references to colour in this figure legend, the reader is referred to the web version of this article.)

errors.

The correlations for the spring flight were generally lower relative to the airborne scenarios A2 and A3. However, the RMSE was similar to the airborne scenarios, indicating that higher error magnitudes were due to the coarser DEM resolution used in the airborne case rather than coarser imagery for the satellite scenarios. Additionally, coarsening the imagery resolution in the spring had a relatively minor impact because the snow surface was more consistent compared to the mixed snow and ice surface in the summer. In contrast, the summer flight had higher errors compared to the airborne scenarios, but the correlation remained high. The higher errors were due to the spatial variability of the glacier surface properties in the summer, which was not as well captured by coarser resolution imagery.

Results for S1_{5nm} and S2_{5nm} (blue and purple triangles in Fig. 6) show that the statistics were generally similar between the coincident and non-coincident DEMs, which indicates that a coincident DEM is less critical at coarser imagery resolution at the glacier scale. This result can also be seen in the BBA difference maps, where the spatial patterns and magnitudes are more similar between S1_{5nm} and S2_{5nm} compared to A2_{5nm} and A3_{5nm} (cf. Figs. 7 and 8). However, localized errors primarily in the ablation zone, where albedo and energy balance are critical for understanding rates of mass balance change, may still be relevant for glacier processes. For example, the large BBA error at the glacier toe in the spring flight, as seen in A3, is still present. Additionally, the summer flight had a large negative albedo error at the snow-glacier ice transition

due to the topography not being correctly represented.

When topography is ignored, high errors exist in all the retrievals with the error being largest for the spring flight due to broader extent of snow cover in the mountain terrain surrounding the glacier (Fig. 9a-b). RF_{LAP} had the largest error of all surface properties whereas grain size was minimally impacted relative to scenarios S1_{5nm} and S2_{5nm}. The direction of the BBA bias covaried with aspect; positive bias on south aspects and negative bias on north aspects (Fig. 9c-d). The error generally increased with increasing slope, though there was no consistent bias direction (Fig. 9e-f). This indicates that error is driven by aspect and slope but exhibits a more consistent relationship with aspect.

6.5. Spectral resolution

Generally, reducing the spectral resolution from 5 nm to 10 nm introduced a small amount of error, (Fig. 6). Error magnitude was stable across both flights, indicating that spectral resolution errors are independent of DEM and imagery resolution error. Additionally, the direction of bias and covariance remained consistent with the 5 nm scenarios. The RF_{LAP} retrieval was less impacted by coarsened spectral resolution than the grain size retrieval, which is likely related to the number of spectral bands used in each of these retrievals. Surprisingly, the grain size retrieval in the summer flight had slightly lower RMSE and higher correlation than the 5 nm retrievals.

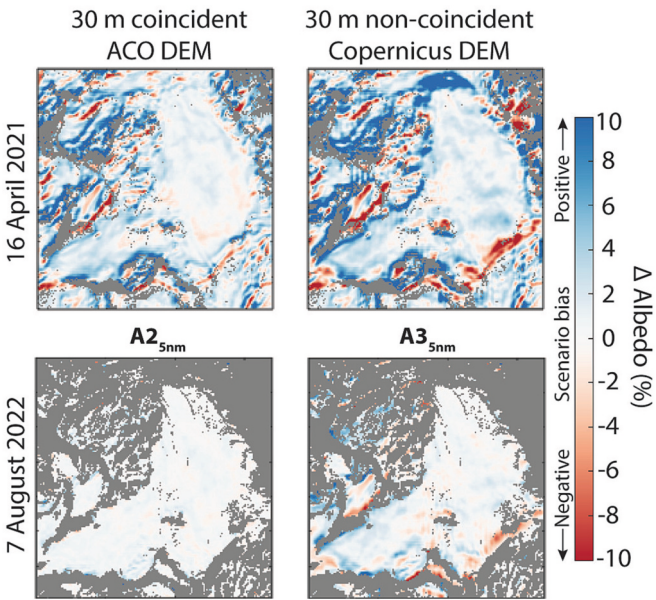


Fig. 7. Spatial comparison of broadband albedo for the spring (top) and summer (bottom) flights from the airborne scenarios $A2_{5\text{nm}}$ (left column) and $A3_{5\text{nm}}$ (right column) against the baseline ACO retrieval $A1_{5\text{nm}}$. Spatial artifacts due to different resolution between the imagery and DEM smoothed with a Gaussian filter after error quantification.

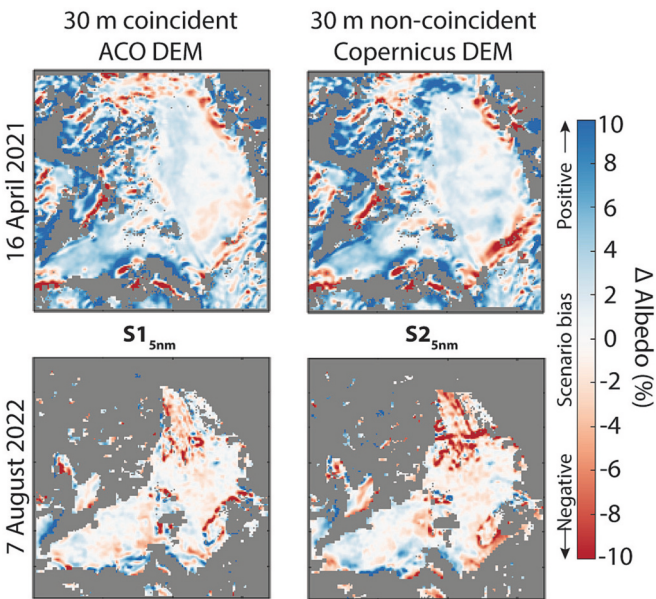


Fig. 8. Spatial comparison of broadband albedo for the spring (top) and summer (bottom) flights from the satellite scenarios $S1_{5\text{nm}}$ (left column) and $S2_{5\text{nm}}$ (right column) against the baseline ACO retrieval $A1_{5\text{nm}}$. Spatial artifacts due to different resolution between the imagery and DEM smoothed with a Gaussian filter after error quantification.

6.6. Mass balance error

With the average BBA from the baseline ACO retrieval we estimate the snow and glacier melt rate using a simple energy analysis, similar to the method presented in Kaspari et al. (2015) and Painter et al. (2013). For each flight date and scenario, we quantify the total error in terms of melt rate based on the BBA RMSE (Table S1). For both flights we assume that the snow and ice is at the melting point (0°C) and that the change in energy due to BBA error goes directly to melt rather than raising the

temperature of the snow or ice. Isothermal snow and ice at 0°C is a reasonable assumption for the surface conditions in the spring and summer flights, which occurred around solar noon. The total net solar into the ice was calculated by multiplying the co-albedo ($1 - \text{BBA}$) by the average incoming solar irradiance that was estimated by ATCOR-4 at the time of flight (900 W m^{-2} and 1020 W m^{-2} for the spring and summer flights, respectively). The estimated melt was calculated by dividing the net solar radiation by the latent heat of fusion of water at 0°C ($0.334 \times 10^6 \text{ J kg}^{-1}$), yielding melt in terms of millimeters water equivalent during one hour (mm w.e. hr^{-1}). The estimated melt from the baseline ACO retrievals were 3.8 and $5.3 \text{ mm w.e. hr}^{-1}$ for the spring and summer flights, respectively. The absolute melt error (%) for each scenario relative to the baseline is summarized in Fig. 10. The lowest melt error was for the baseline scenario with coarser spectral resolution, 0.12 and $0.09 \text{ mm w.e. hr}^{-1}$ (3% and 2% error) in spring and summer, respectively. Spectral resolution was negligible for the other scenarios and were not included in Fig. 10.

Corresponding to higher surface retrieval error, the melt error was also higher for the spring flight, even with lower incoming solar irradiance. The error magnitude was similar for the airborne and satellite scenarios that used a 30 m DEM (0.65 – $0.76 \text{ mm w.e. hr}^{-1}$ or 17% – 20% error; Fig. 10). As expected, though, the coincident DEM scenarios had slightly lower error relative to the non-coincident DEM scenarios regardless of imagery resolution. The non-coincident DEM scenarios ($A3$ and $S2$) had similar error (0.76 and $0.75 \text{ mm w.e. hr}^{-1}$ or 20% error) meaning that the coarsened imagery did not introduce additional error at the glacier scale. The highest error was for the no DEM scenario ($1.19 \text{ mm w.e. hr}^{-1}$ or 31% error).

The melt error was lower for the summer flights, although there was a larger difference between the airborne (0.18 – $0.30 \text{ mm w.e. hr}^{-1}$ or 3% – 6% error) and satellite scenarios (0.58 and $0.59 \text{ mm w.e. hr}^{-1}$ or 11% error). This indicates that imagery resolution played a larger role in melt error in the summer when the surface conditions were more variable. The highest melt error across the summer flights was again for the no DEM scenario ($0.67 \text{ mm w.e. hr}^{-1}$ or 13% error), although it was not much higher than the other satellite scenarios, showing that neglecting topography had lower impact relative to the spring flight. Overall, this analysis demonstrates that seemingly small errors in BBA can produce relatively large errors in net solar radiation and melt.

7. Discussion

7.1. Baseline retrieval uncertainty

Although the baseline ACO retrievals were used as the reference from which all other scenarios were assessed, they too have their own uncertainties. Since ground validation was not collected during the two flights presented, we rely on the reported uncertainties from the IS-SnARF algorithm as an estimate. We do, however, expect our retrievals uncertainties to be lower comparatively because the fine-resolution coincidentally collected DEM was used for topographic correction, whereas the IS-SnARF algorithm used a globally available 30 m DEM. In Painter et al. (2013) they also used the rural aerosol model in atmospheric correction and assumed the uncertainty introduced by this was low, due to low aerosol optical depth measured at the high elevation mountain study area. In comparing spectral reflectance output from ATCOR-4 to coincident field spectrometer observations, the spectrum RMSE was 0.015 for soil and 0.014 for snow.

The grain size retrieval error over snow using a similar fitting parameter over the ice absorption feature was also estimated at ± 20 – $50 \mu\text{m}$ for grain sizes 50 – $900 \mu\text{m}$ following Nolin and Dozier (Nolin and Dozier, 2000). Uncertainty in grain size propagates to uncertainties in BBA and RF_{LAP} because it determines the anisotropy factor that is selected and the reference spectral albedo from which the RF_{LAP} is calculated, these were reported to at ± 0.0001 for BBA and ± 3.8 for RF_{LAP} . Relative to in situ observations, the actual differences between

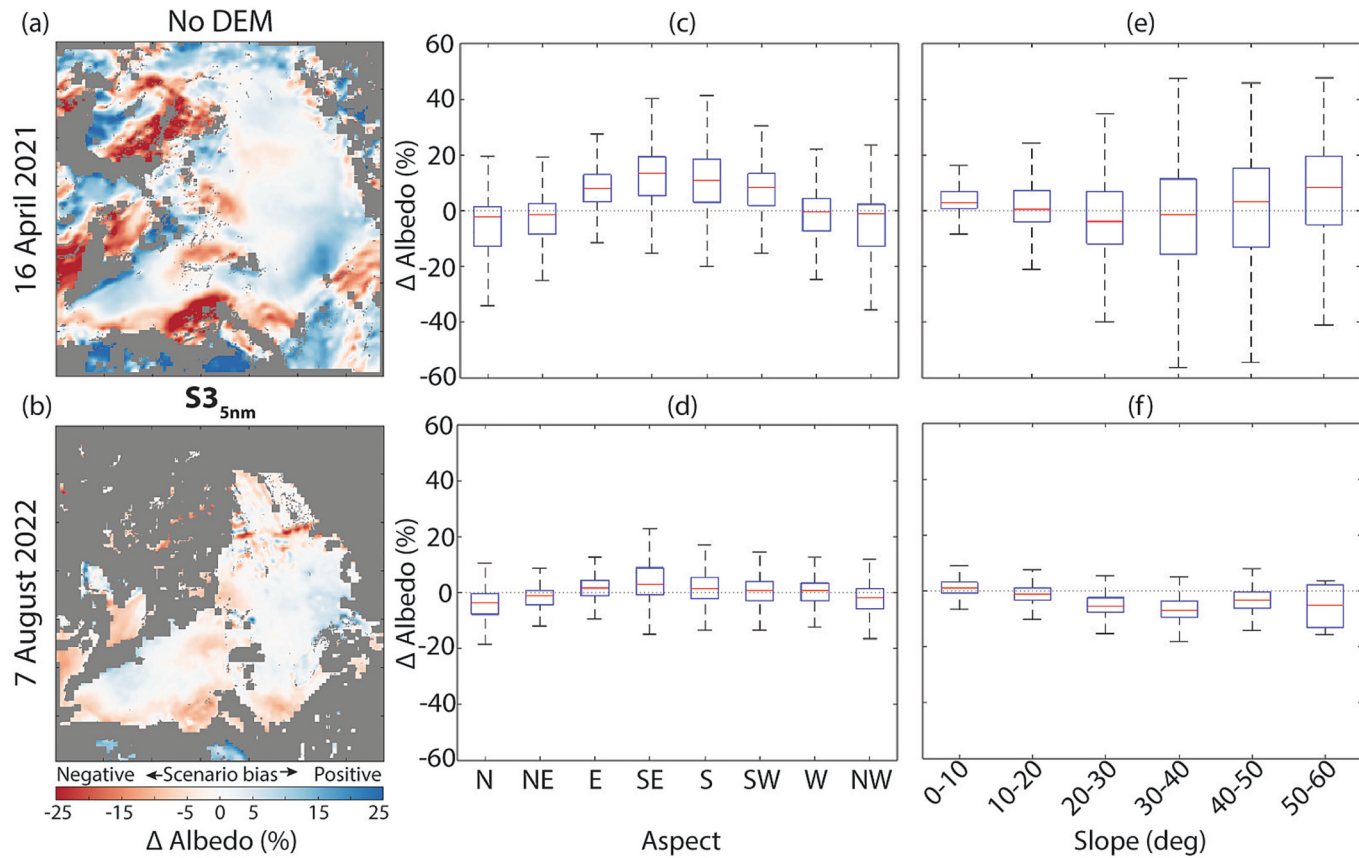


Fig. 9. Spatial comparison of broadband albedo for the spring (a) and summer (b) flights from the satellite scenario S3_{5nm} against the baseline ACO retrieval A1_{5nm}. The BBA scale bar was increased to $\pm 25\%$, relative to $\pm 10\%$ in Figs. 7 and 8, to capture the greater magnitude of error. Spatial artifacts due to different resolution between the imagery and DEM smoothed with a Gaussian filter after error quantification. The albedo error from a and b are plotted in terms of aspect (c-d) and slope (e-f).

retrieval and observations of BBA was 0.001–0.004 and RF_{LAP} was 2.1 $\pm 5.1 \text{ W m}^{-2}$. The uncertainties due specifically to sensor noise were reported to be $\pm 3.6 \text{ W m}^{-2}$, ± 0.001 , and $\pm 0.2 \text{ W m}^{-2}$ for grain size, BBA, and RF_{LAP} respectively (Painter et al., 2013).

7.2. DEM resolution and topographic correction

Our results show that, compared to a 2 m DEM, use of 30 m DEMs yielded larger errors in BBA and RF_{LAP} retrievals. Topography distorts the measured radiance at the sensor, which the topographic correction attempts to correct. The spectra distortion is not uniform across the visible and NIR regions; in the visible wavelengths the shape and magnitude are affected, whereas in the NIR region only the magnitude is affected (Carmon et al., 2023; Fig. 2). Higher error for RF_{LAP} and BBA was thus expected because they are most influenced by the magnitude and shape of the measured reflectance spectrum across the visible wavelengths, where solar flux is also greatest. Additionally, the spectral reflectance distortion manifests as a downward “hooking” shape that can imitate impacts from LAPs (e.g., Fig. 2).

Grain size had a lower contribution to BBA error using the coarse DEM, which was due to illumination geometry primarily impacting the magnitude of the NIR region. Since the grain size retrieval is based on the normalized depth and shape of the absorption feature (Fig. 2), a change in absolute magnitude has a smaller impact on the retrieval. Compared to the errors in RF_{LAP}, grain size errors translated to smaller errors in net solar radiation. For example, the spring flight max RF_{LAP} RMSE was 62.6 W m^{-2} , whereas the max grain size RMSE (155 μm) would translate into $\pm 13.0 \text{ W m}^{-2}$ in net solar radiation for the average solar irradiance during the flight. Similarly, for the summer flight the

max RF_{LAP} RMSE was 38 W m^{-2} , whereas the max grain size RMSE (326 μm) would translate into $\pm 16.3 \text{ W m}^{-2}$ for net solar radiation.

The timing of DEM acquisition was important for localized areas that experience frequent change, such as in the ablation zone. Between the time of the Copernicus and ACO DEM acquisitions the glacier had receded and caused BBA error around the glacier toe. With rapid increase in glacier retreat rates in recent years, this is an important consideration for future imaging spectroscopy studies that rely on globally available DEMs. Further, this demonstrates the need for more frequent DEM acquisitions globally.

7.3. Spectral resolution

The coarsening from 5 to 10 nm spectral resolution had little effect on total retrieval errors, and in the case of grain size, performed best. The BBA and RF_{LAP} retrievals integrate over many bands making them less susceptible to the reduced spectral resolution if the signal to noise ratio is maintained. The grain size retrieval uses the minimum band depth in the absorption feature and the apparent minimum can shift slightly with the lower spectral resolution. However, the grain size differences between the spectral resolution scenarios have a minimal impact on BBA. This finding could be a concern though for instruments with coarser than 10 nm spectral resolution. In this case, alternatives that leverage multiple bands should be used, such as spectral fitting to the right side of the absorption feature (Seidel et al., 2016), or for dry snow conditions that use the scaled band area approach of Nolin and Dozier (2000).

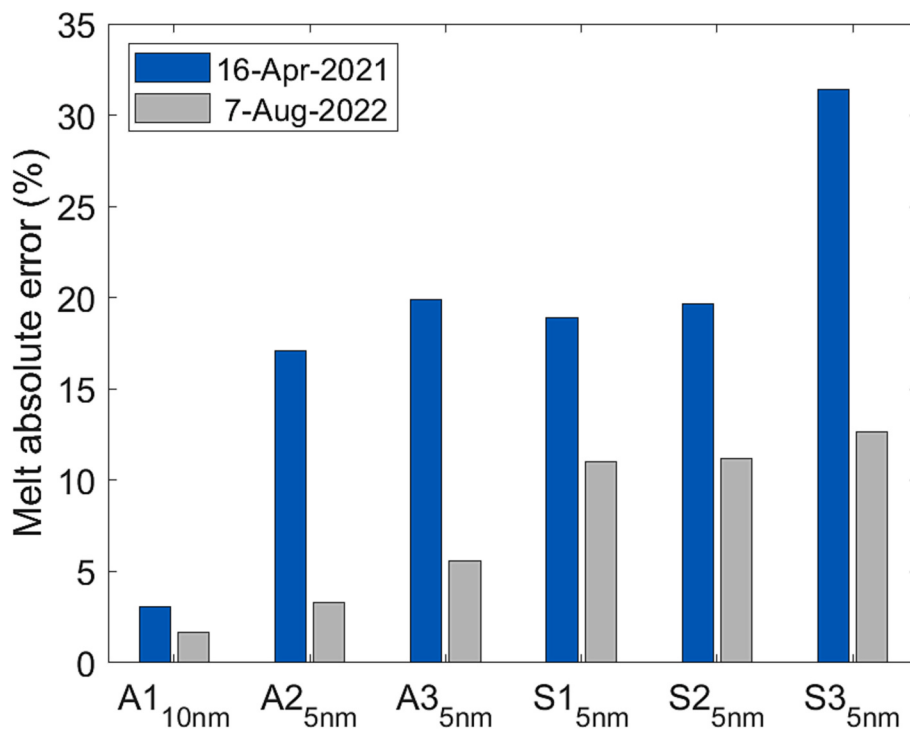


Fig. 10. Melt absolute error over one hour for each 5 nm spectral resolution scenario. All the 10 nm spectral resolution scenarios were excluded, except for the baseline retrieval (A1_{10nm}).

7.4. Implications for energy and mass balance modeling

Spatially distributed energy and mass balance modeling predominately use ‘time since snowfall’ albedo decay functions to calculate net solar radiation over snow and a constant albedo for glacier ice (Hock, 2005). Simple diagnostic representations are not realistic and propagate errors in melt timing and magnitude (Meyer et al., 2023). Despite the important role albedo plays for glacier melt rates this approach has remained essentially the same for decades because there are few albedo measurements from which albedo representations can be parameterized, and those that are developed from in situ observations are only applicable locally. Case studies show that updating albedo using observations from airborne and spaceborne spectrometers better represents albedo decay and improves seasonal snowmelt (Bair et al., 2019; Molotch et al., 2004) and glacier mass balance (Dumont et al., 2012b). These studies demonstrate the value of representing the observed spatial and temporal variability in albedo and indicate that as imaging spectroscopy retrievals increase in availability there will be much needed improvements in this critical energy balance parameter. Retrievals that use non-coincident DEMs for topographic correction, though, should expect greater error around the glacier terminus and snow-glacier ice transitions zones. This is an important result because these errors will translate to melt error over the areas of the glacier where most of the mass loss is occurring.

7.5. Considerations for future work

Within the next decade, consistent global coverage of spectral reflectance from satellite imaging spectroscopy is expected. It is thus necessary to understand what the associated error and uncertainty will be for snow and ice surface property retrievals prior to the start of this new data record. The scenarios presented here are based upon our best understanding of the instrument characteristics in terms of spatial and spectral resolution. Based on the retrieval algorithm (ISSIA) and remote sensing scales analyzed in this study, a few general recommendations can be made for snow and ice surface property retrieval from satellite

and airborne imaging spectroscopy.

- i. Spectral resolution of 10 nm was adequate for the retrievals presented here (i.e., BBA, grain size, and RF_{LAP}) based on the error in BBA being <0.2% compared to the equivalent 5 nm resolution scenario. Other surface property retrievals that rely on small spectral features could benefit from having 5 nm spectral resolution, such as retrievals for algae or differentiating dust and black carbon concentrations. These types of retrievals, however, leverage the visible region of the spectrum only.
- ii. For satellite sensors, errors from topographic correction using a 30 m resolution DEM are similar between the non-coincident and coincident DEMs indicating that at the glacier scale a coincident DEM is not critical. For higher resolution imagery, as in the airborne scenarios, having a coincident DEM was more important.
- iii. Retrievals in glacier ablation zones using a non-coincident DEM may have higher error and should be used with caution in energy and mass balance models.
- iv. Since the two baseline ACO retrievals were collected under ideal clear sky conditions close to solar noon, additional uncertainties should be expected from satellite imaging spectrometers due to illumination conditions, clouds, and atmospheric conditions.

8. Conclusion

We presented snow and ice surface property retrievals from the ACO (i.e., BBA, grain size, and RF_{LAP}) over Place Glacier, British Columbia, Canada. Our ISSIA algorithm is based on the IS-SnARF workflow (Painter et al., 2013), with key modifications that increased the suitability for retrievals over perennial snow, firn, and glacier ice. The two flights are representative of typical spring and summer conditions for mountain glaciers in Western Canada, which was reflected in the surface property retrievals. The BBA was 8.9% lower for the summer flight, which we attribute to RF_{LAP} being 21.2 W m⁻² higher and grain sizes being 826 μm larger relative to the spring flight. The exposed extent of

bare ice at the glacier toe, which is significantly darker than snow, contributed to the higher average RF_{LAP} and grain size for the summer flight.

Synthetic datasets were generated from the fine-resolution baseline ACO retrievals to quantify expected errors for other coarser resolution airborne and satellite remote sensing platforms. Using a coarsened 30 m DEM introduced the most error during the spring flight, where the surrounding mountains were snow covered, impacting the BBA and RF_{LAP} retrievals more than the grain size retrieval. Although the DEM introduced errors in the summer flight as well, they were generally lower because the snow cover was limited to less complex glaciated terrain. Non-coincident global DEM introduced more errors when applied to fine resolution imagery relative to the coarser imagery. There were, however, large errors in the ablation zone due to mass loss that was not captured in the non-coincident DEM. The coarser imagery resolution for the satellite scenarios did not fully capture spatial variability in surface properties and topography, which lowered the variance and increased RMSE. Finally, reducing the spectral resolution from 5 nm to 10 nm only minimally impacted the retrievals and the error was independent of DEM or imagery resolution.

Funding statement

This work was supported by the Tula Foundation, the National Sciences and Engineering Research Council of Canada, and the Canada Research Chairs Program.

CRediT authorship contribution statement

Christopher P. Donahue: Conceptualization, Methodology, Software, Validation, Formal analysis, Investigation, Data curation, Visualization, Writing – original draft, Writing – review & editing. **Brian Menounos:** Conceptualization, Writing – review & editing, Resources, Supervision, Project administration, Funding acquisition. **Nick Viner:** Software, Data curation. **S. McKenzie Skiles:** Methodology, Writing – review & editing. **Steven Beffort:** Data curation. **Taylor Denouden:** Data curation. **Santiago Gonzalez Arriola:** Data curation. **Robert White:** Data curation. **Derek Heathfield:** Data curation, Visualization, Supervision, Project administration.

Declaration of Competing Interest

The authors declare no conflict of interest.

Data availability

The Imaging Spectroscopy Snow and Ice Algorithm (ISSIA) is available as a MATLAB script on GitHub (<https://github.com/donahuechristopher/ISSIA>).

The baseline 2 m ACO retrievals (i.e., broadband albedo, grain size, radiative forcing by LAPs) for both flight dates along with the coincidentally collected 2 m DEM are available here: <https://doi.org/10.6084/m9.figshare.22777184>.

The Copernicus global DEM is distributed by Open Topography (<https://opentopography.org>).

Acknowledgements

We thank Jeff Dozier and two anonymous referees for their insightful reviews that helped improve this manuscript.

Appendix A. Supplementary data

Supplementary data to this article can be found online at <https://doi.org/10.1016/j.rse.2023.113849>.

References

- Abolafia-Rosenzweig, R., He, C., McKenzie Skiles, S., Chen, F., Gochis, D., 2022. Evaluation and optimization of snow albedo scheme in Noah-MP land surface model using in situ spectral observations in the Colorado Rockies. *J. Adv. Model. Earth Syst.* 14, e2022MS003141 <https://doi.org/10.1029/2022MS003141>.
- Asner, G.P., Knapp, D.E., Kennedy-Bowdoin, T., Jones, M.O., Martin, R.E., Boardman, J. W., Field, C.B., 2007. Carnegie airborne observatory: in-flight fusion of hyperspectral imaging and waveform light detection and ranging for three-dimensional studies of ecosystems. *J. Appl. Remote. Sens.* 1, 013536 <https://doi.org/10.1117/1.2794018>.
- Bair, E.H., Dozier, J., Stern, C., LeWinter, A., Rittger, K., Savagian, A., Stillinger, T., Davis, R.E., 2022. Divergence of apparent and intrinsic snow albedo over a season at a sub-alpine site with implications for remote sensing. *Cryosphere* 16, 1765–1778. <https://doi.org/10.5194/tc-16-1765-2022>.
- Bair, E.H., Rittger, K., Skiles, S.M., Dozier, J., 2019. An examination of snow albedo estimates from MODIS and their impact on snow water equivalent reconstruction. *Water Resour. Res.* 55, 7826–7842. <https://doi.org/10.1029/2019WR024810>.
- Bair, E.H., Stillinger, T., Dozier, J., 2020. Snow property inversion from remote sensing (SPIREs): a generalized multispectral unmixing approach with examples from MODIS and landsat 8 OLI. *IEEE Trans. Geosci. Remote Sens.* <https://doi.org/10.1109/TGRS.2020.3040328>.
- Bohn, N., Di Mauro, B., Colombo, R., Thompson, D.R., Susiluoto, J., Carmon, N., Turmon, M.J., Guanter, L., 2022. Glacier ice surface properties in south-West Greenland ice sheet: first estimates from PRISMA imaging spectroscopy data. *J. Geophys. Res. Biogeosciences* 127, e2021JG006718. <https://doi.org/10.1029/2021JG006718>.
- Bohn, N., Painter, T.H., Thompson, D.R., Carmon, N., Susiluoto, J., Turmon, M.J., Helminger, M.C., Green, R.O., Cook, J.M., Guanter, L., 2021. Optimal estimation of snow and ice surface parameters from imaging spectroscopy measurements. *Remote Sens. Environ.* 264, 112613 <https://doi.org/10.1016/j.rse.2021.112613>.
- Bohren, C.F., Huffman, D.R., 1998. Absorption and Scattering of Light by Small Particles. John Wiley and Sons, Inc, New York. <https://doi.org/10.1002/9783527618156>.
- Calonne, N., Flin, F., Geindreau, C., Lessaffre, B., Rolland du Roscoat, S., 2014. Study of a temperature gradient metamorphism of snow from 3-D images: time evolution of microstructures, physical properties and their associated anisotropy. *Cryosphere* 8, 2255–2274. <https://doi.org/10.5194/tc-8-2255-2014>.
- Carmon, N., Berk, A., Bohn, N., Brodrick, P.G., Dozier, J., Johnson, M., Miller, C.E., Thompson, D.R., Turmon, M., Bachmann, C.M., 2023. Shape from spectra. *Remote Sens. Environ.* 288, 113497 <https://doi.org/10.1016/j.rse.2023.113497>.
- Cawse-Nicholson, K., Townsend, P.A., Schimel, D., Assiri, A.M., Blake, P.L., Buongiorno, M.F., Campbell, P., Carmon, N., Casey, K.A., Correa-Pabón, R.E., 2021. NASA's surface biology and geology designated observable: a perspective on surface imaging algorithms. *Remote Sens. Environ.* 257, 112349 <https://doi.org/10.1016/j.rse.2021.112349>.
- Chabrillat, S., Guanter, L., Segl, K., Foerster, S., Fischer, S., Rossner, G., Schickling, A., LaPorta, L., Honold, H.-P., Storch, T., 2020. The Enmap German spaceborne imaging spectroscopy mission: Update and highlights of recent preparatory activities. In: Presented at the IGARSS 2020-2020 IEEE International Geoscience and Remote Sensing Symposium. IEEE, pp. 3278–3281. <https://doi.org/10.1109/IGARSS39084.2020.9324006>.
- Clark, R.N., Roush, T.L., 1984. Reflectance spectroscopy: quantitative analysis techniques for remote sensing applications. *J. Geophys. Res.* 89, 6329–6340. <https://doi.org/10.1029/JB089iB07p06329>.
- Cogliati, S., Sarti, F., Chiariantini, L., Cosi, M., Lorusso, R., Lopinto, E., Miglietta, F., Genesio, L., Guanter, L., Damm, A., 2021. The PRISMA imaging spectroscopy mission: overview and first performance analysis. *Remote Sens. Environ.* 262, 112499 <https://doi.org/10.1016/j.rse.2021.112499>.
- Connelly, D.S., Thompson, D.R., Mahowald, N.M., Li, L., Carmon, N., Okin, G.S., Green, R.O., 2021. The EMIT mission: information yield for mineral dust radiative forcing. *Remote Sens. Environ.* 258, 112380 <https://doi.org/10.1016/j.rse.2021.112380>.
- DeWalle, D.R., Rango, A., 2008. Principles of snow hydrology. Cambridge University Press, Cambridge. <https://doi.org/10.1017/CBO9780511535673>.
- Donahue, C., Skiles, S.M., Hammonds, K., 2022. Mapping liquid water content in snow at the millimeter scale: an intercomparison of mixed-phase optical property models using hyperspectral imaging and in situ measurements. *Cryosphere* 16, 43–59. <https://doi.org/10.5194/tc-16-43-2022>.
- Donahue, C., Skiles, S.M., Hammonds, K., 2021. In situ effective snow grain size mapping using a compact hyperspectral imager. *J. Glaciol.* 67, 49–57. <https://doi.org/10.1017/jog.2020.68>.
- Dozier, J., 1989. Spectral signature of alpine snow cover from the landsat thematic mapper. *Remote Sens. Environ.* 28, 9–22. [https://doi.org/10.1016/0034-4257\(89\)90101-6](https://doi.org/10.1016/0034-4257(89)90101-6).
- Dozier, J., Bair, E.H., Baskaran, L., Brodrick, P.G., Carmon, N., Kokaly, R.F., Miller, C.E., Miner, K.R., Painter, T.H., Thompson, D.R., 2022. Error and uncertainty degrade

- topographic corrections of remotely sensed data. *J. Geophys. Res. Biogeosci.* 127, e2022JG007147. <https://doi.org/10.1029/2022JG007147>.
- Dozier, J., Marks, D., 1987. Snow mapping and classification from landsat thematic mapper data. *Ann. Glaciol.* 9, 97–103. <https://doi.org/10.3189/S026030550000046X>.
- Dumont, M., Brissaud, O., Picard, G., Schmitt, B., Gallet, J.-C., Arnaud, Y., 2010. High-accuracy measurements of snow bidirectional reflectance distribution function at visible and NIR wavelengths—comparison with modelling results. *Atmos. Chem. Phys.* 10, 2507–2520. <https://doi.org/10.5194/acp-10-2507-2010>.
- Dumont, Marie, Durand, Y., Arnaud, Y., Six, D., 2012b. Variational assimilation of albedo in a snowpack model and reconstruction of the spatial mass-balance distribution of an alpine glacier. *J. Glaciol.* 58, 151–164. <https://doi.org/10.3189/2012JoG11J163>.
- Dumont, M., Gardelle, J., Sirguey, P., Guillot, A., Six, D., Rabatel, A., Arnaud, Y., 2012a. Linking glacier annual mass balance and glacier albedo retrieved from MODIS data. *Cryosphere* 6, 1527–1539. <https://doi.org/10.5194/tc-6-1527-2012>.
- European Space Agency, S., 2021. Copernicus Global Digital Elevation Model. Distributed by OpenTopography.
- Fair, Z., Flanner, M., Schneider, A., Skiles, S.M., 2022. Sensitivity of modeled snow grain size retrievals to solar geometry, snow particle asphericity, and snowpack impurities. *EGUphere* 1–22. <https://doi.org/10.5194/tc-16-3801-2022>.
- Flanner, M.G., Arnheim, J.B., Cook, J.M., Dang, C., He, C., Huang, X., Singh, D., Skiles, S. M., Whicker, C.A., Zender, C.S., 2021. SNICAR-ADv3: a community tool for modeling spectral snow albedo. *Geosci. Model Dev.* 14, 7673–7704. <https://doi.org/10.5194/gmd-14-7673-2021>.
- Gardner, A.S., Sharp, M.J., 2010. A review of snow and ice albedo and the development of a new physically based broadband albedo parameterization. *J. Geophys. Res. Earth Surf.* 115. <https://doi.org/10.1029/2009JF001444>.
- Gergely, M., Wolfsperger, F., Schneebeli, M., 2013. Simulation and validation of the InfraSnow: an instrument to measure snow optically equivalent grain size. *IEEE Trans. Geosci. Remote Sens.* 52, 4236–4247. <https://doi.org/10.1109/TGRS.2013.2280502>.
- Green, R.O., Painter, T.H., Roberts, D.A., Dozier, J., 2006. Measuring the expressed abundance of the three phases of water with an imaging spectrometer over melting snow. *Water Resour. Res.* 42, W10402. <https://doi.org/10.1029/2005WR004509>.
- Hall, D.K., Riggs, G.A., Salomonson, V.V., 1995. Development of methods for mapping global snow cover using moderate resolution imaging spectroradiometer data. *Remote Sens. Environ.* 54, 127–140. [https://doi.org/10.1016/0034-4257\(95\)00137-P](https://doi.org/10.1016/0034-4257(95)00137-P).
- Hock, R., 2005. Glacier melt: a review of processes and their modelling. *Prog. Phys. Geogr.* 29, 362–391. <https://doi.org/10.1191/0309133305 pp453ra>.
- Hock, R., Rasul, G., Adler, C., Cáceres, B., Gruber, S., Hirabayashi, Y., Jackson, M., Kääb, A., Kang, S., Kutuzov, S., 2019. High mountain areas. In: Pörtner, H.-O., Roberts, D.C., Masson-Delmotte, V., Zhai, P., Tignor, M. (Eds.), *IPCC Special Report on the Ocean and Cryosphere in a Changing Climate*, pp. 131–202. <https://doi.org/10.1017/9781009157964.004>.
- Hotaling, S., Lutz, S., Dial, R.J., Anesio, A.M., Benning, L.G., Fountain, A.G., Kelley, J.L., McCutcheon, J., Skiles, S.M., Takeuchi, N., 2021. Biological albedo reduction on ice sheets, glaciers, and snowfields. *Earth-Sci. Rev.* 220, 103728. <https://doi.org/10.1016/j.earscirev.2021.103728>.
- Hugonet, R., McNabb, R., Berthier, E., Menounos, B., Nuth, C., Girod, L., Farinotti, D., Huss, M., Dussaillant, I., Brun, F., 2021. Accelerated global glacier mass loss in the early twenty-first century. *Nature* 592, 726–731. <https://doi.org/10.1038/s41586-021-03436-z>.
- Jin, Z., Charlock, T.P., Yang, P., Xie, Y., Miller, W., 2008. Snow optical properties for different particle shapes with application to snow grain size retrieval and MODIS/CERES radiance comparison over Antarctica. *Remote Sens. Environ.* 112, 3563–3581. <https://doi.org/10.1016/j.rse.2008.04.011>.
- Johnson, B.R., Kuester, M.A., Kampe, T.U., Keller, M., 2010. National ecological observatory network (NEON) airborne remote measurements of vegetation canopy biochemistry and structure. In: Presented at the 2010 IEEE International Geoscience and Remote Sensing Symposium. IEEE, pp. 2079–2082. <https://doi.org/10.1109/IGARSS.2010.5654121>.
- Kaempfer, T.U., Schneebeli, M., 2007. Observation of isothermal metamorphism of new snow and interpretation as a sintering process. *J. Geophys. Res. Atmos.* 112. <https://doi.org/10.1029/2007JD009047>.
- Kaspari, S., Skiles, S.M., Delaney, I., Dixon, D., Painter, T.H., 2015. Accelerated glacier melt on snow dome, mt. Olympus, Washington, USA due to deposition of black carbon and mineral dust from wildfire. *J. Geophys. Res. Atmos.* <https://doi.org/10.1002/2014jd022676>.
- Kokhanovsky, A., Di Mauro, B., Colombo, R., 2022. Snow surface properties derived from PRISMA satellite data over the nansen ice shelf (East Antarctica). *Front. Environ. Sci.* 1420. <https://doi.org/10.3389/fenvs.2022.904585>.
- Kokhanovsky, A.A., Zege, E.P., 2004. Scattering optics of snow. *Appl. Opt.* 43, 1589–1602. <https://doi.org/10.1364/AO.43.001589>.
- Larue, F., Picard, G., Arnaud, L., Ollivier, I., Delcourt, C., Lamare, M., Tuzet, F., Revuelto, J., Dumont, M., 2020. Snow albedo sensitivity to macroscopic surface roughness using a new ray-tracing model. *Cryosphere* 14, 1651–1672. <https://doi.org/10.5194/tc-14-1651-2020>.
- Libois, Q., Picard, G., France, J., Arnaud, L., Dumont, M., Carmagnola, C., King, M., 2013. Influence of grain shape on light penetration in snow. *Cryosphere* 7, 1803. <https://doi.org/10.5194/tc-7-1803-2013>.
- Marks, D., Dozier, J., 1992. Climate and energy exchange at the snow surface in the alpine region of the Sierra Nevada 2. Snow cover energy balance. *Water Resour. Res.* 28, 3043–3054. <https://doi.org/10.1029/92WR01483>.
- Meyer, J., Horel, J., Kormos, P., Hedrick, A., Trujillo, E., Skiles, S.M., 2023. Operational water forecast ability of the HRRR-iSnobal combination: an evaluation to adapt into production environments. *Geosci. Model Dev.* 16, 233–250. <https://doi.org/10.5194/gmd-16-233-2023>.
- Minder, J.R., Letcher, T.W., Skiles, S.M., 2016. An evaluation of high-resolution regional climate model simulations of snow cover and albedo over the Rocky Mountains, with implications for the simulated snow-albedo feedback. *J. Geophys. Res. Atmos.* 121, 9069–9088. <https://doi.org/10.1002/2016JD024995>.
- Mishchenko, M., Dlugach, J.M., Yanovitskij, E.G., Zakharov, N.T., 1999. Bidirectional reflectance of flat, optically thick particulate layers: an efficient radiative transfer solution and applications to snow and soil surfaces. *J. Quant. Spectrosc. Radiat. Transf.* 63, 409–432. [https://doi.org/10.1016/S0022-4073\(99\)00028-X](https://doi.org/10.1016/S0022-4073(99)00028-X).
- Molotch, N., Painter, T.H., Bales, R., Dozier, J., 2004. Incorporating remotely sensed snow albedo into a spatially distributed snowmelt model. *Geophys. Res. Lett.* 31. <https://doi.org/10.1029/2003GL019063>.
- Mukherjee, K., Menounos, B., Shea, J., Mortezapour, M., Ednie, M., Demuth, M.N., 2022. Evaluation of surface mass-balance records using geodetic data and physically-based modelling, place and peyto glaciers, western Canada. *J. Glaciol.* 1–18. <https://doi.org/10.1017/jog.2022.83>.
- Müller, R., Avbelj, J., Carmona, E., Gerasch, B., Graham, L., Günther, B., Heiden, U., Kerr, G., Knott, U., Krutz, D., 2016. The new hyperspectral sensor DESIS on the multi-payload platform MUSES installed on the ISS. *Int. Arch. Photogramm. Remote Sens. Spat. Inf. Sci.* 41, 461–467. <https://doi.org/10.5194/isprs-archives-XLI-B1-461-2016>.
- Nolin, A.W., Dozier, J., 2000. A hyperspectral method for remotely sensing the grain size of snow. *Remote Sens. Environ.* 74, 207–216. [https://doi.org/10.1016/S0034-4257\(00\)00111-5](https://doi.org/10.1016/S0034-4257(00)00111-5).
- Oerlemans, J., Giesen, R., Van den Broeke, M., 2009. Retreating alpine glaciers: increased melt rates due to accumulation of dust (Vadret da morteratsch, Switzerland). *J. Glaciol.* 55, 729–736. <https://doi.org/10.3189/002214309789470969>.
- Oerlemans, J., Knap, W., 1998. A 1 year record of global radiation and albedo in the ablation zone of Morteratschgletersche, Switzerland. *J. Glaciol.* 44, 231–238. <https://doi.org/10.3189/S0022143000002574>.
- Painter, T.H., Barrett, A.P., Landry, C.C., Neff, J.C., Cassidy, M.P., Lawrence, C.R., McBride, K.E., Farmer, G.L., 2007. Impact of disturbed desert soils on duration of mountain snow cover. *Geophys. Res. Lett.* 34. <https://doi.org/10.1029/2007GL030284>.
- Painter, T.H., Berisford, D.F., Boardman, J.W., Bormann, K.J., Deems, J.S., Gehrke, F., Hedrick, A., Joyce, M., Laidlaw, R., Marks, D., Skiles, S.M., 2016. The airborne snow observatory: fusion of scanning lidar, imaging spectrometer, and physically-based modeling for mapping snow water equivalent and snow albedo. *Remote Sens. Environ.* 184, 139–152. <https://doi.org/10.1016/j.rse.2016.06.018>.
- Painter, T.H., Rittger, K., McKenzie, C., Slaughter, P., Davis, R.E., Dozier, J., 2009. Retrieval of subpixel snow covered area, grain size, and albedo from MODIS. *Remote Sens. Environ.* 113, 868–879. <https://doi.org/10.1016/j.rse.2009.01.001>.
- Painter, T.H., Seidel, F., Skiles, S.M., Bryant, A., Rittger, K., 2013. Imaging spectroscopy of albedo and radiative forcing by light absorbing impurities in mountain snow. *J. Geophys. Res. Atmos.* 118. <https://doi.org/10.1002/jgrd.50520>.
- Pelto, B.M., Menounos, B., Marshall, S.J., 2019. Multi-year evaluation of airborne geodetic surveys to estimate seasonal mass balance, Columbia and Rocky Mountains, Canada. *Cryosphere* 13, 1709–1727. <https://doi.org/10.5194/tc-13-1709-2019>.
- Rast, M., Nieke, J., Adams, J., Isola, C., Gascon, F., 2021. Copernicus hyperspectral imaging mission for the environment (chime). In: Presented at the 2021 IEEE International Geoscience and Remote Sensing Symposium IGARSS. IEEE, pp. 108–111. <https://doi.org/10.1109/IGARSS47720.2021.9553319>.
- RGI Consortium, 2017. Randolph glacier inventory - a dataset of global glacier outlines. Version 6. <https://doi.org/10.7265/4mlf-gd79>.
- Richter, R., Schläpfer, D., 2011. Atmospheric/topographic correction for airborne imagery. In: ATCOR-4 User Guide. https://www.rese-apps.com/pdf/atcor4_manual.pdf.
- Rounce, D.R., Hock, R., Maussion, F., Hugonet, R., Kochtitzky, W., Huss, M., Berthier, E., Brinkerhoff, D., Compagni, L., Copland, L., 2023. Global glacier change in the 21st century: every increase in temperature matters. *Science* 379, 78–83. <https://doi.org/10.1126/science.abo1324>.
- Schaepman-Strub, G., Schaepman, M., Painter, T.H., Dangel, S., Martonchik, J.V., 2006. Reflectance quantities in optical remote sensing - definitions and case studies. *Remote Sens. Environ.* 103, 27–42. <https://doi.org/10.1016/j.rse.2006.03.002>.
- Seidel, F.C., Rittger, K., Skiles, S.M., Molotch, N.P., Painter, T.H., 2016. Case study of spatial and temporal variability of snow cover, grain size, albedo and radiative forcing in the Sierra Nevada and Rocky Mountain snowpack derived from imaging spectroscopy. *Cryosphere* 10, 1229–1244. <https://doi.org/10.5194/tc-10-1229-2016>.
- Skiles, S.M., Donahue, C., Hunsaker, A., Jacobs, J., 2023. UAV hyperspectral imaging for multiscale assessment of landsat 9 snow grain size and albedo. *Front. Remote Sens.* 3, 110. <https://doi.org/10.3389/frsen.2022.103827>.
- Skiles, S.M., Flanner, M.G., Cook, J., Dumont, M., Painter, T.H., 2018. Radiative forcing by light absorbing particles in snow. *Nat. Clim. Change.* <https://doi.org/10.1038/s41558-018-0296-5>.

- Skiles, S.M., Painter, T.H., 2019. Toward understanding direct absorption and grain size feedbacks by dust radiative forcing in snow with coupled snow physical and radiative transfer modeling. *Water Resour. Res.* <https://doi.org/10.1029/2018WR024573>.
- Skiles, S.M., Painter, T.H., 2017. Daily evolution in dust and black carbon content, snow grain size, and snow albedo during snowmelt, Rocky Mountains, Colorado. *J. Glaciol.* 63, 118–132. <https://doi.org/10.1017/jog.2016.125>.
- Stamnes, K., Tsay, S.-C., Wiscombe, W.J., Jayaweera, K., 1988. Numerically stable algorithm for discrete-ordinate-method radiative transfer in multiple scattering and emitting layered media. *Appl. Opt.* 27, 2502–2509. <https://doi.org/10.1364/AO.27.002502>.
- Stavros, E.N., Chrone, J., Cawse-Nicholson, K., Freeman, A., Glenn, N.F., Guild, L., Kokaly, R., Lee, C., Luval, J., Pavlick, R., 2023. Designing an observing system to study the surface biology and geology (SBG) of the earth in the 2020s. *J. Geophys. Res. Biogeosciences* 128, e2021JG006471. <https://doi.org/10.1029/2021JG006471>.
- Taylor, K.E., 2001. Summarizing multiple aspects of model performance in a single diagram. *J. Geophys. Res. Atmos.* 106, 7183–7192. <https://doi.org/10.1029/2000JD900719>.
- Warren, S.G., Wiscombe, W.J., 1980. A model for the spectral albedo of snow, II, snow containing atmospheric aerosols. *J. Atmos. Sci.* 37, 2734–2745. [https://doi.org/10.1175/1520-0469\(1980\)037<2734:AMFTSA>2.0.CO;2](https://doi.org/10.1175/1520-0469(1980)037<2734:AMFTSA>2.0.CO;2).